Contributions to the Analysis and Design of Mechanical Systems for a Series Hybrid Chevrolet Camaro

Jan Wittenbecher

A thesis

submitted in partial fulfillment of the

requirements for the degree of

Master of Science in Mechanical Engineering

University of Washington

2017

Committee:

Brain C. Fabien, Chair

Per G. Reinhall

Philip C. Malte

Program Authorized to Offer Degree:

Department of Mechanical Engineering

University of Washington

Abstract

Contributions to the Analysis and Design of Mechanical Systems for a Series Hybrid Chevrolet Camaro

Jan Wittenbecher

Chair of the Supervisory Committee: Professor Brian C. Fabien
Department of Mechanical Engineering

Plug-in hybrid electric vehicles use a powertrain architecture that includes components of traditional powertrains such as internal combustion engines and transmissions, as well as components found in battery electric vehicles. The combination of both technologies enables vehicles to drive emission free, when using the battery as the energy source, while also providing the typical long driving range offered by traditional combustion engines using liquid fuel as the energy source. The goal of this study is to contribute to the design and analysis of machine elements and components used in a series plug-in hybrid vehicle. This vehicle was built for the University of Washington's team that competes in the EcoCAR 3 Advanced Vehicle Technology Competition. A motorcycle combustion engine was used in the generator system of the vehicle, and a CAE software GT-Power model was used to analyze the engine's fuel efficiency. Approximations and estimations of model parameters were used to predict the fluid dynamics, combustion process, energy conversion and heat transfer occurring in the engine. Speed and engine load are varied over a broad range to establish a map for brake specific fuel consumption which is data of value for the development of an optimal generator control strategy. The electric drivetrain used in the series hybrid involves single speed reduction gearboxes between motors and drive shafts. Static and fatigue strength analysis is performed to evaluate the strength of an undersized gearbox part for the re-specification of the material and heat treatment used to increase the part's strength to an acceptable level. The increased number of powertrain components used in hybrid vehicles, particularly the electric battery, lead to an increased vehicle rear mass. This is accommodated for in the analysis of the vehicle's rear suspension and the design of a new set of coil springs.

Acknowledgments

The successful completion of the University of Washington's EcoCAR project is due to the help and support of a number of people and institutions.

I would like to thank Professor Brian C. Fabien for giving me the opportunity to join the EcoCAR team and especially for his advice and guidance during this project. I would also like to thank my EcoCAR lab mates: James Goin, Aman Kalia, Rachel Krause, Nicholas Christoforou, and Siyuan Liu; the student machine shop leads Eamon McQuaide and Reginald Rocamora; and the entire mechanical team for all their support and hard work during Year 3 by turning various ideas and designs into a functioning vehicle. This work would not have been possible without the support and advice of the EcoCAR 3 Advanced Vehicle Technology Competition sponsors including: General Motors, the U.S. Department of Energy, the Argonne National Laboratory, and other competition and team based sponsors.

Finally, I would like to thank my wife, Rebekah, who has been my greatest supporter and motivator during my time in graduate school.

Table of Contents

List of Figures

List of Tables

List of Nomenclature

General Symbols

Symbol	First Used in Section	Description
A	2.3.2	Anchor angle
A_r	2.3.3	Valve train curtain area
BDC	2.3.3	Bottom Dead Center
BSFC	2.2	Brake Specific Fuel Consumption
C	2.3.2	Wiebe constant
C_d	2.3.3	Discharge coefficient
$c_{p,m}$	2.3.1	Mean piston speed
DC	1.3	Direct Current
D	2.3.2	Duration
d_d	4.1.3	Damper damping rate
d_t	4.1.3	Tire damping rate
D_v	2.3.3	Valve area
E	2.3.2	Wiebe exponent
$F_{s,stock}$ $F_{s,new}$	4.2.2	Spring load, stock and new
FMEP	2.3.1	Friction Mean Effective Pressure
f_n	4.2.1	Natural frequency
k_a through k_f	3.2.5	Marine factor a through f
K_f	3.2.5	Fatigue stress concentration factor
k_r	4.2.1	Ride rate
k_s, $k_{s,new}$	4.1.3	Coil spring rate, new
k_t	4.1.3	Tire spring rate
k_w	4.2.1	Wheel rate
K_{ts}	3.2.3	Torsional stress concentration factor

K_t	3.2.3	Bending stress concentration factor
L_v	2.3.3	Valve lift area
l_0, l_1	4.2.2	Spring length, free and compressed
m_{2P}	4.2.1	Mass of two front passages
N	3.2.5	Number of cycles
n_y	3.2.3	Factor of safety for first cycle failure
n_f	3.2.5	Fatigue factor of safety
SOC	1.3	State of Charge
TDC	2.3.1	Top Dead Center
P	4.1.1	Front ride height
q	3.2.5	Notch sensitivity factor
T	3.2.2	Torque
R	4.1.1	Rear ride height
r	4.1.3	Coil spring motion ratio
S	2.3.2	Start of combustion
S_e	3.2.5	Design endurance limit
S'_e	3.2.5	Material endurance limit
S_y	3.2	Yield strength
S_{ut}	3.2.5	Ultimate tensile strength
x_b	2.3.2	Mass fraction burned

Unit Symbols

Symbol	First Used in Section	Description
A	1.3	Ampere
°C	2.2	Degrees Celsius
cm^3	2.1	Cubic centimeter

HB	3.2.4	Hardness Brinell scale
HHV	2.4.2	Higher Heating Value
hp	1.3	Horse power
HRC	3.2	Hardness Rockwell C scale
K	2.3.1	Kelvin
kg	2.4.2	Kilogram
kW	1.3	Kilowatt
kWh	1.3	Kilowatt hour
L	2.3.4	Liter
lb-ft	1.3	Pound-foot
mi	1.3	Mile
MJ	2.4.2	Mega Joule
mm	2.1	Millimeter
mph	3.1	Miles per hour
MPa	3.2	Megapascal
N	3.2.2	Newton
N_2	2.3.1	Nitrogen
Nm	1.3	Newton meter
O_2	2.3.1	Oxygen
rpm	1.1	Rounds per minute
s	1.3	Second
V	1.3	Volt

Greek Symbols

Symbol	First Used in Section	Description
$\beta_{1,}\ \beta_{2,}$	3.2.2	Angle 1 and 2 in Constant Velocity Joints
τ	3.2.3	Shear stress
σ	3.2.3	Normal stress

1 INTRODUCTION

1.1 Motivation

Redesigning the powertrain architecture of a series production vehicle, from traditional internal combustion engine to hybrid electric, requires changes to many key vehicle components. The process involves many aspects of engineering, mechanical engineering in particular. The complexity of a hybrid powertrain is significantly increased compared to a traditional powertrain and many additional components: electric motors, battery packs, and power electronics, are packaged in the same limited space. Typically, this leads to an increased vehicle mass compared to non-hybrid counterparts, motivating mechanical engineers to reengineer the vehicle suspension parameters. The use of traditional propulsion components like combustion engines and transmissions in hybrid applications impacts the engineering requirements for these components. In a traditional powertrain, the speed of the internal combustion engine depends upon vehicle speed and transmission gears, while the load depends on the driver's torque demand and road loads. In hybrid vehicles, series hybrids in particular, the combustion engine speed and load are independent from vehicle speed and driver input. Control engineers have a great deal of freedom as a result, to develop electronic engine control strategies using ideal engine set points for energy efficiency and emissions by analyzing the engine's fuel consumption and emissions characteristics. Internal combustion engines, used for vehicle propulsion, offer a limited bandwidth of operational speeds in which they can deliver torque, typically ranging from about 800 rpm to 6000 rpm. This requires multi speed transmissions in order to match the minimum engine speed to the smallest desired vehicle speed in the smallest gear, and maximum engine speed to the highest desired vehicle speed in the highest gear. Electric motors used for vehicle propulsion do not have comparable limitations as they can deliver torque at 0 rpm motor speed and typically provide a higher ratio of peak torque to peak power than combustion engines; making the use of multispeed transmissions unnecessary. A simple single speed transmission is typically sufficient to match the maximum motor speed to the maximum vehicle speed. Mechanical engineers are then motivated to design compact and lightweight single speed automotive transmissions, providing the reliability and durability needed for this application.

1.2 Overview of the EcoCAR 3 Competition

EcoCAR 3 is an Advanced Vehicle Technology Competition (AVTC) between 16 university student teams in North America. The competition is managed by Argonne National Laboratory and sponsored by the U.S. Department of Energy and General Motors Corporation. [1] The competition's goal is to redesign a 2016 Chevrolet Camaro in order to reduce its environmental impact while maintaining its performance. This is achieved through hybridization of the car's powertrain and the use of alternative fuels. Students working in these teams have four years (2014 through 2018) to redesign, manufacture, integrate, validate and optimize energy efficient powertrains with minimal help from faculty and industry advisors. The car's original body design and safety features must be retained. The University of Washington (UW) EcoCAR 3 team consists of approximately 85 students across multiple academic disciplines, all working together with the goal of creating a unique vehicle that breaks away from conventional powertrain configurations reflected in the vehicle architecture choice.

1.3 UW EcoCAR 3 Vehicle Architecture.

The architecture of UW's Camaro is a Series Plug-in Hybrid Electric Vehicle (PHEV). Team-designed subassemblies can be seen in **Figure 1-1**.

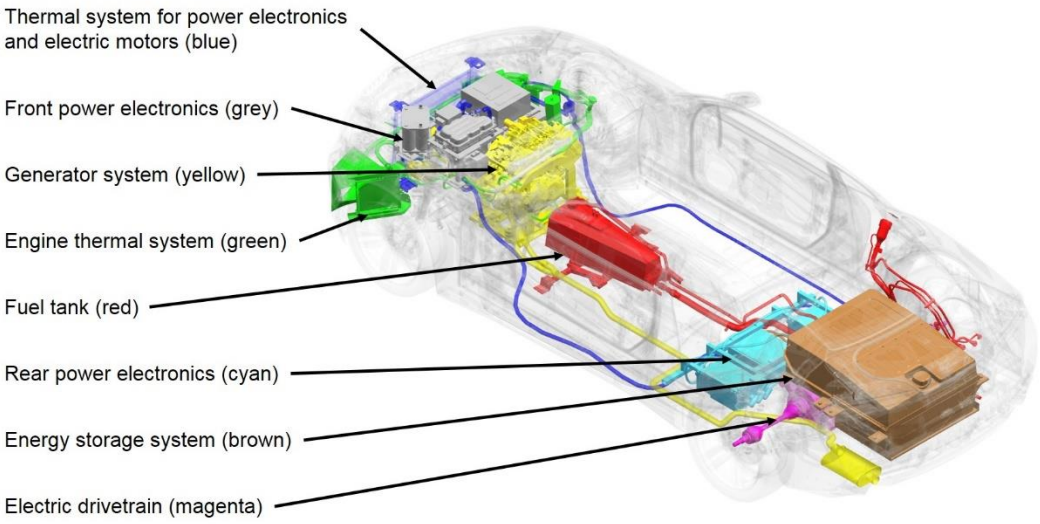

Figure 1-1: UW Camaro with team-designed subassemblies

The rear of the vehicle hosts two Emrax 268 axial-flux traction motors, one motor for each rear wheel. The motors are coupled to team-designed planetary gearboxes and controlled by a Unitek Bamocar D3 700-400-RS motor controller. Electric energy is fed to the controllers from an A123 7x15s3p battery package, also called Energy Storage System (ESS). The ESS has a capacity of 18.9 kWh and a nominal voltage of 340 V. Its lithium iron-phosphate cell chemistry allows for a high peak discharge rate of 600 A, necessary to satisfy the power demand of the traction motors. The front of the vehicle contains a generator unit consisting of an engine, mechanically coupled to a motor-generator for generation of electric energy. The engine is a 2002 Honda VFR 800 motorcycle engine modified to run with E85 fuel. The engine's built-in 6 speed manual transmission is retained but configured to operate in a single gear speed. The motorcycle's original chain drive is replaced by a disc coupler to mate the engine with a motor-generator. The motor-generator is a Bosch SMG 180 is controlled by a Bosch INVCON 2.3 motor controller with integrated 12 V DC-DC converter module. The powertrain diagram for the series torque vectored (Series-TV) architecture can be found in **Figure 1-2**, a list of all powertrain components used can be found in **Table 1-1** and a list of vehicle specifications in **Table 1-2.**

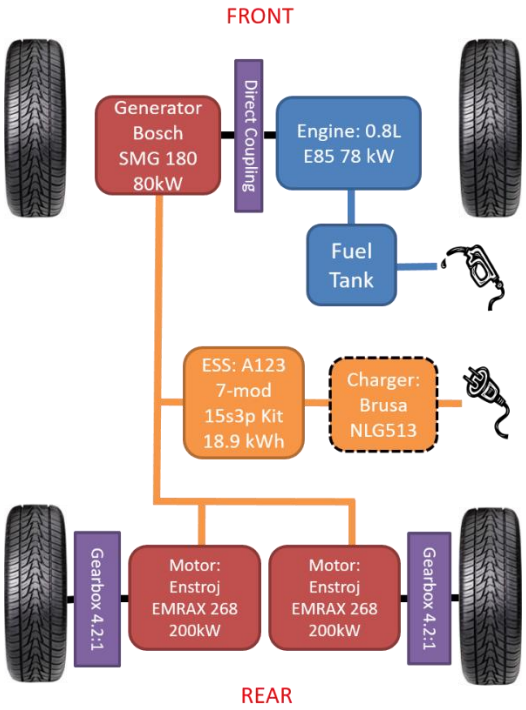

Figure 1-2: UW Series-TV architecture

Table 1-1: Component performance specifications

Component	Manufacturer/Model	Specification
Traction motor	Emrax 268	230 kW peak power nominal (limited by inverters) 500 Nm peak torque
Inverter for traction motor	Unitek Bamocar D3 400	140 kW peak power
Motor-generator	Bosch SMG 180	80 kW peak power
Generator motor controller	Bosch INVCON Gen 2.3	85 kW peak power
Gearboxes	Team-designed	Gear ratio: 4.2
Engine	2002 Honda VFR 800	78 kW maximum power
ESS	A123 7x15s3p ESS	18.9 kWh, 600 Amp peak discharge, 340 V nominal

The vehicle has three different drive modes:

- Charge Depleting (CD) mode: The vehicle solely uses the battery charge for propulsion while the generator system remains out of operation. Typically used when the ESS state of charge (SOC) is high at the beginning of a trip.
- Charge Sustaining (CS) mode: The generator system is used to charge the battery while the vehicle is in operation. This mode is automatically triggered when the SOC falls below 20% in the CD-mode, alternatively it can be requested manually by the driver at any SOC lower than 100%.
- Performance mode: The generator system operated at maximum power output to provide additional current to the electric drive motors. This is intended to support short term peaks in power demand.

This series architecture enables performance gains compared to the stock vehicle but also allows for efficient generator system control when performance driving mode is not desired.

Table 1-2: Vehicle specification in comparison

Specification	UW	Stock Camaro	Camaro SS
Total power (hp)	353	275	455
Total torque (lb-ft)	750	295	455
Power-to-weight ratio (kW/kg)	0.1477	0.1357	0.2028
Engine displacement (L)	0.8	2.0	6.2
IMV-60 mph (sec)	6.3	5.5	4.0
ESS capacity (kWh)	18.9	-	-
EV range (mi)	50	-	-
Useable ESS capacity (%SOC)	10-100%	-	-
CD-mode fuel consumption (Wh/km)	0	-	-
CD-mode electric energy consumption (Wh/km)	180	-	-
CS-mode fuel consumption (Wh/km)	256	-	-
Total energy consumption	436Wh/km	22/31 mpg	17/28 mpg

2 FUEL EFFICIENCY OF A MOTORCYCLE ENGINE

2.1 Mechanical Design of the Generator System

Details of the generator system are provided in this section. The Honda VFR 800 spark ignition engine has four cylinders in a 90° V configuration with a total displacement of 782 cm^3 and comes with a built-in clutch and 6-speed manual transmission. For the generation of electric power a disk coupler is flanged onto the transmission output of the engine to provide the mechanical coupling to a Bosch SMG 180. **Figure 2-1** and **Figure 2-2** show Computer aided design (CAD) images of the generator system setup with its support structure.

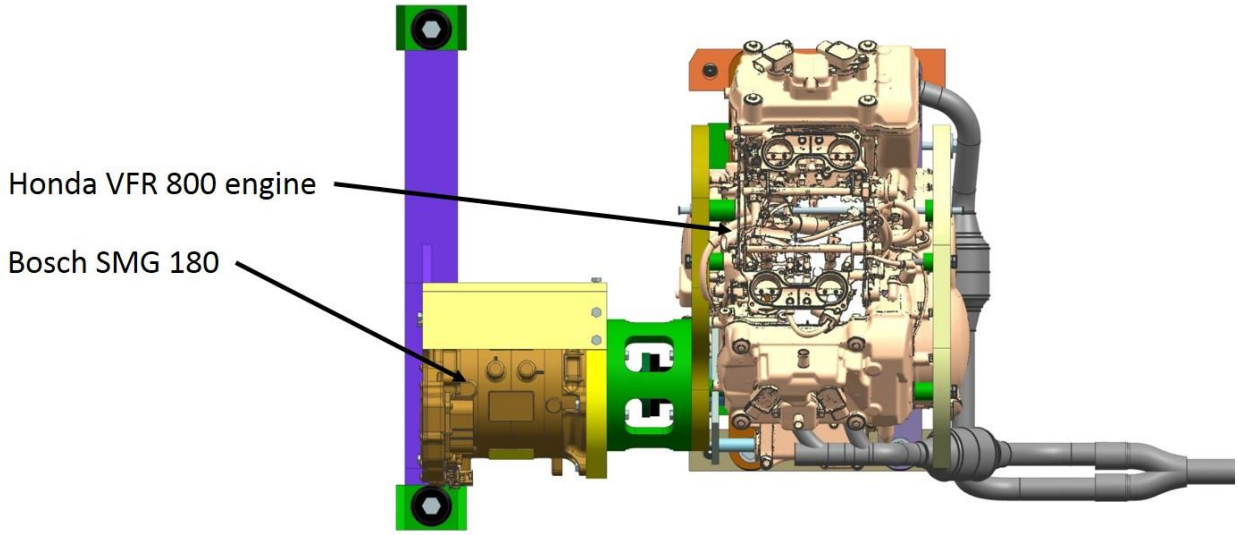

Figure 2-1: Generator system assembly, top view

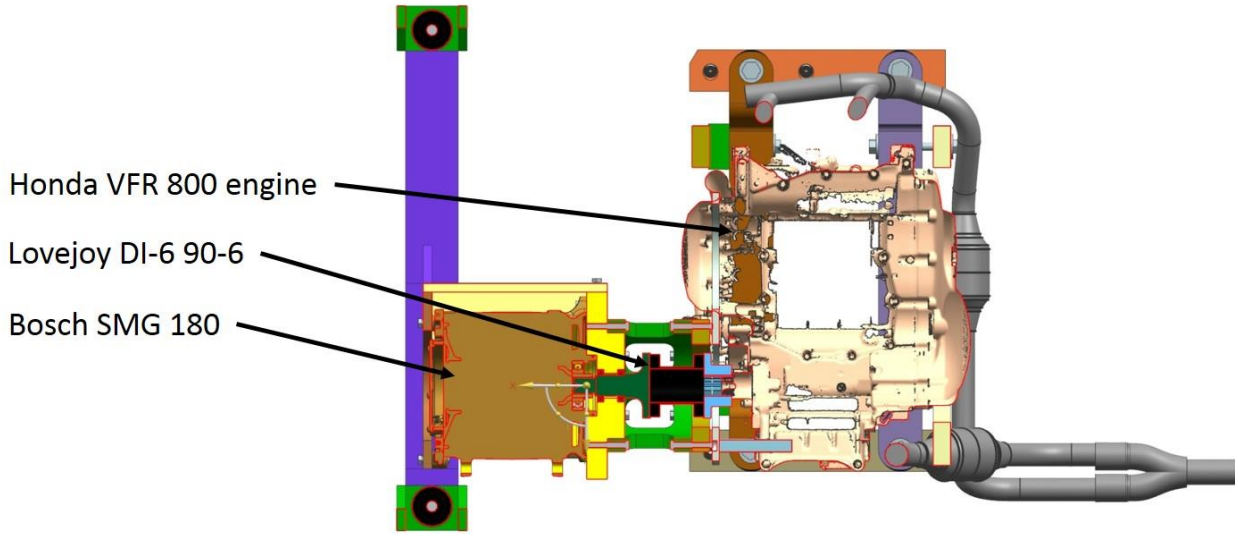

Figure 2-2: Generator system assembly, cross section

In the motorcycle, the transmission output drives a sprocket for the final chain drive and this drives the rear wheel. This chain drive arrangement doesn't require any alignment features; thus, it is not necessary for the engine to provide any of these features at its output shaft. In the generator system application, the engine's output directly drives the generator and is sensitive to misalignment. A flexible disk coupler is used to adjust for any misalignment between the engine and the motor-generator. This disk coupler is a Lovejoy DI-6, model 90-6, specifications can be found in **Table 2-1**.

Table 2-1: Lovejoy DI-6 90-6 specifications

Torque		Max Speed		Maximum Misalignment	
Nominal	Peak	Unbalanced	Balanced	Axial	Angular
240 Nm	480 Nm	9,100 rpm	22,700 rpm	1.5 mm	1.5°

2.2 Gear Selection

The engine's internal transmission provides the necessary reduction ratio between the engine and the motor-generator and matches the speed and torque characteristic of both components. During operation, it is intended that the transmission is to remain in the same gear selected for vehicle drive mode needs. For the charge sustaining mode, gear selection is driven by maximum fuel efficiency for the desired power output. In this mode power output will be limited by the continuous charge limit of the ESS which is 60 A. Given the nominal 340 V this results in a maximum continuous charging power of 20.4 kW. The torque and power characteristics of the engine and the motor-generator can be found in **Figure 2-3** and **Figure 2-4.** For stationary generator system operation, the motor-generator has to be capable of delivering equal, or more, torque than the engine puts out to the motor-generator shaft. Maximum engine power output is handled by the motor-generator in the engine's 4th, 5th and 6th gears using the motor-generator's peak torque capabilities. At 75 °C coolant temperature peak torque can be sustaining for at least 25 seconds before derating. During performance driving mode, this is sufficient to support power demand during acceleration.

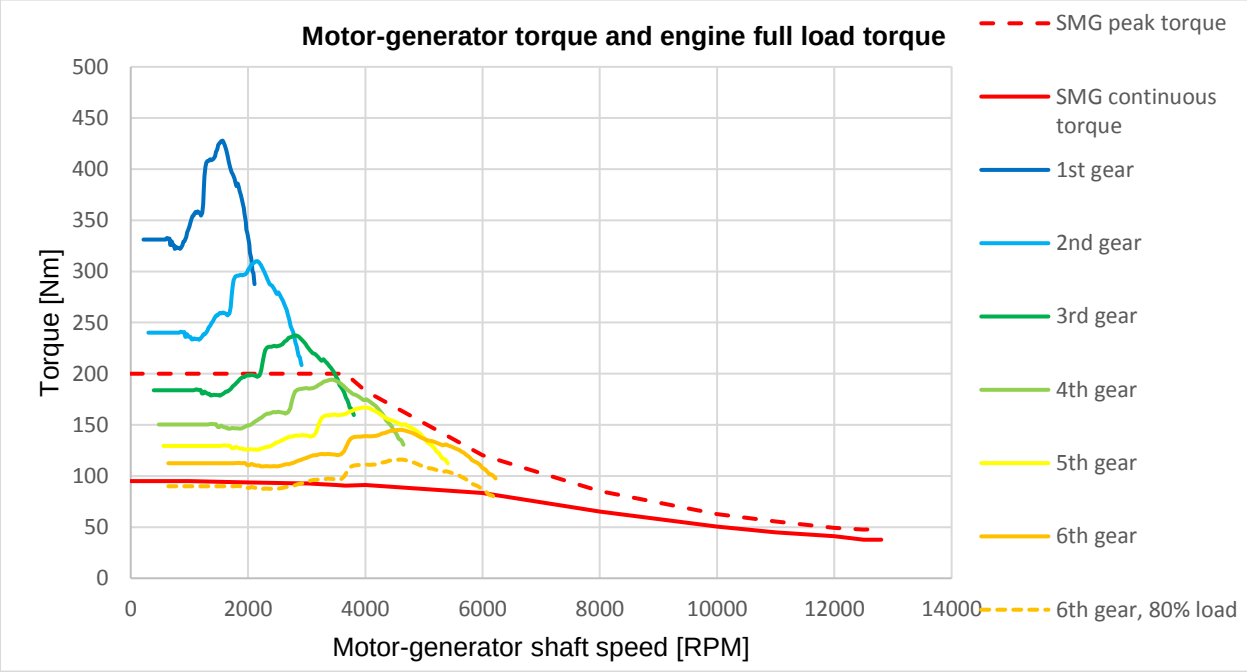

Figure 2-3: Motor-generator and engine torque characteristics. Motor-generator numbers are based on manufacture specifications, engine numbers are based on brake torque dynamometer testing with a maximum error of ± 5%.

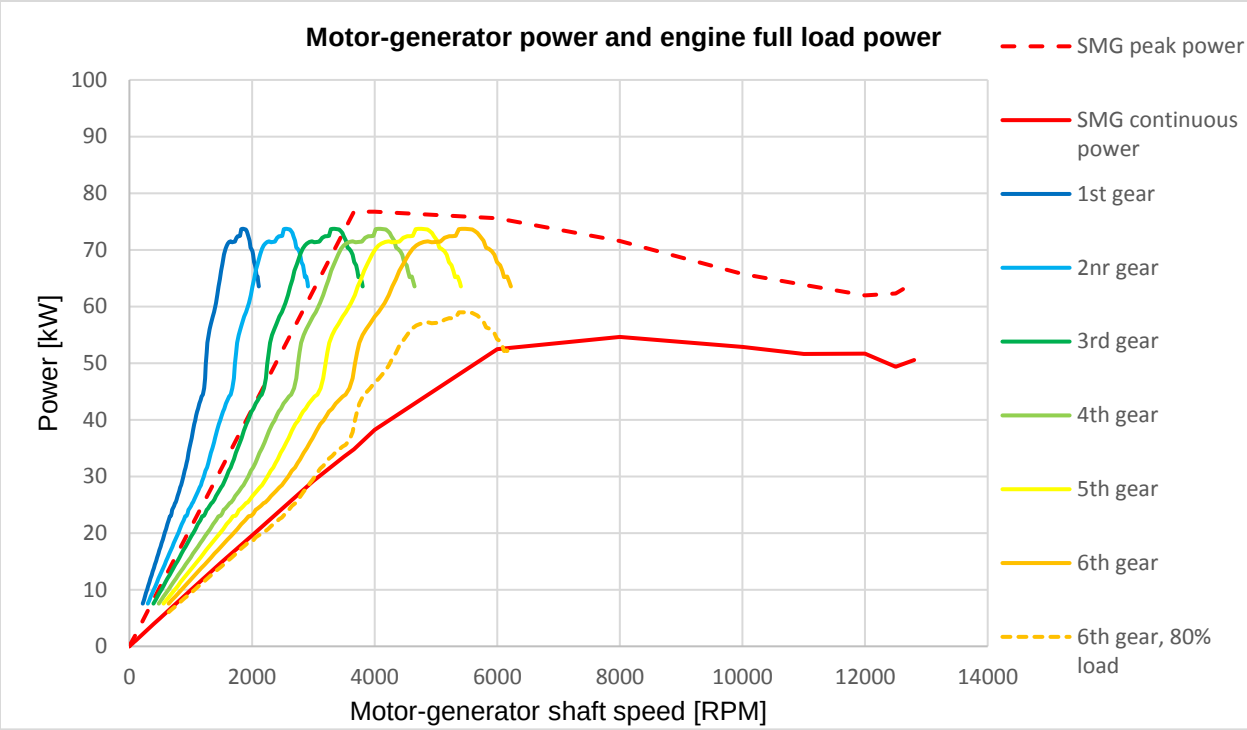

Figure 2-4: Motor-generator and engine power characteristics. Motor-generator are numbers based on manufacture specifications, engine are numbers based on brake torque dynamometer testing with a maximum error of ± 5%.

In charge sustaining mode, the generator system is operated at a constant power output for an extended period of time. This requires the engine's torque output to be lower than the motor-generator's continuous torque in the desired engine set point. Even in 6th gear this requires the engine to be operated below full load. 80% load or lower allows a continuous output of at least 25 kW. The data suggests that the 6th gear is the desired gear for all drive modes. The exact engine set point in the charge sustaining mode will be determined by the goal of maximizing fuel efficiency. In the following chapter the engine's brake specific fuel efficiency (BSFC) will be analyzed in a GT-Power model to determine the optimal set point.

2.3 Engine modeling in GT-Power

The Computer Aided Engineering (CAE) tool GT-Power is used to simulate engine performance to predict performance quantities such as power, torque airflow, volumetric efficiency, fuel consumption, pumping losses, etc. It can also be used to predict tailpipe emissions, intake and exhaust acoustic behavior, in-cylinder, intake and manifold temperature, and in-cylinder pressure [2]. The modeling format of GT-Power is object-oriented. It comprises three levels of hierarchy: templates, objects and parts. Templates for common engine components are provided by the software. These are made into objects by defining parameters needed by the models within the program. Objects are made into parts when they are placed on the project map. They inherit parameters from their parent objects. A typical engine model uses the component objects “EngineCrankTrain”, “EngineCylinder” and the connection object “ValveCamConn” to define the basic geometry and characteristics of the engine. Component and connection objects may refer to several reference objects defining aspects like combustion, fluid composition and fuel properties [3]. Major objects and parts used for modeling the Honda VFR 800 motorcycle engine are described in the chapters that follow. Parameters used in the model are generally taken from three sources:

- The official Honda VFR 800/A Interceptor Service Manual
- Measurements take of the physical engine and the
- The GT-SUITE Engine Performance Application Manual, Version 2017

2.3.1 Cranktrain

The “EngineCrankTrain” object uses reference objects to define cylinder geometry and engine friction. The engine friction object is used to model the mechanical friction loads of the engine. When experimental data is not available GT-Power uses a Chen-Flynn model [4] which describes a speed and pressure dependent Friction Mean Effective Pressure (FMEP) as follows:

$$FMEP = FMEP_{const} + A \cdot P_{cycle,max} + B \cdot c_{p,m} + C \cdot {c_{p,m}}^2 \tag{2.1}$$

Table 2-2: Engine friction parameters

Variable definition		Value in model
$FMEP_{const}$	Constant part of FMEP	0.4 bar *
A	Peak cylinder pressure factor	0.005 *
$P_{cycle,max}$	Maximum cylinder pressure	Calculated by model solver
B	Mean piston speed factor	0.09 bar/(m/s) *
$c_{p,m}$	Mean piston speed	Calculated by model solver
C	Mean piston speed squared factor	9e-4 bar/(m/s)^2 *
* Recommended values for 4-stroke engines [5]		

The cylinder geometry object defines the basic engine design parameters. The Honda VFR 800 engine has an over-square stroke ratio reducing the mean piston speed at high engine speeds and allowing for relatively large valves and air intake cross-sections. Its rather unusual 90°-V4 configuration leads to firing intervals different from the typical, even, 180° in inline-four cylinders. Cylinders #1 and #3 comprise one cylinder bank and cylinders #2 and #4 comprise the other bank.

Table 2-3: Cylinder geometry and firing order

Parameter	Value in model
Bore	72 mm *
Stroke	48 mm *
Connecting Rod Length	100 mm (estimated)
Compression Ratio	11.6 *
TDC Clearance Height	1 mm (estimated)
Firing order	#1-180°-#3-270°-#2-180°-#4-90°-#1 *
* Values from the official Honda VFR 800/A Interceptor Service Manual	

The “EngineCrankTrain” also uses a reference object as a reference state for the volumetric efficiency. For this model, it is called “initial” and is defined as air at 1 bar absolute pressure and 300 K temperature. Air is defined as a mixture of 0.767 N_2-vapor and 0.233 O_2-vapor in terms of mass fractions. This reference object is used in a number of engine objects, in parts on the intake side and inside the engine to initialize the model in the first cycle.

2.3.2 Cylinders

The “EngineCylinder” object specifies attributes of the engine cylinders using a number of reference objects. The initial fluid state is defined by the object described above. The wall temperature object defines the temperatures for the head, cylinder and piston. Experimental data for temperature is not available, thus the temperatures used in the model are typical for liquid cooled engines under full load operation. The heat transfer object which describes the heat transfer inside the cylinder uses a heat transfer model called WoschniGT and is similar to the classical Woschni correlation without swirl [6], except when open valves increase the fluid velocity. The use of this model is recommended when measured swirl data is not available [5].

Table 2-4: Parameters used wall temperature and heat transfer objects

Parameter	Value in model
Head temperature	550 K *
Piston temperature	590 K *
Cylinder temperature	450 K *
Heat Transfer Model	WoschniGT *
Head/Bore Area Ratio	1.15 **
Piston/Bore Area Ratio	1 **
* Recommended values from [5] ** Estimated values for Honda VFR 800	

The 'EngCylComb” object specifies the in-cylinder combustion model. Predictive and non-predictive combustion models are available in GT-Power. Predictive models like “EngCylCombSITurb” will predict the

combustion burn rate and emissions based on a turbulent flame model. Experimental combustion data is not required, but spark timing and flow data inside the cylinder must be obtained. A simple "EngCylCombSIWiebe" is used for the Honda VFR800 engine performance model. It defines the combustion process using a Wiebe function. For the greatest accuracy, the Wiebe function can be fitted to experimental combustion data obtained from measured in-cylinder pressure traces. Pressure traces are not available in this case and typical values for spark ignition engines are used instead [3]. Assuming the fuel burns completely during combustion (combustion efficiency equal to 1) the Wiebe function for instantaneous crank angle θ is defined as follows [5]:

$$x_b(\theta) = 1 - \exp[-(C)(\theta - S)^{E+1}] \tag{2.2}$$

$$C = \left[\frac{D}{-ln(0.1)^{1/(E+1)} + ln(0.1)^{1/(E+1)}}\right]^{-(E+1)} \tag{2.3}$$

$$S = \mathrm{A} - \frac{D(-\ln(0.5))^{1/(E+1)}}{-ln(0.1)^{1/(E+1)} + ln(0.1)^{1/(E+1)}} \tag{2.4}$$

Table 2-5: Parameters used by the "EngCylCombSIWiebe" reference object

Variable definition		Value in model
x_b	Mass fraction burned	Calculated by model
A	Anchor Angle (50% burn), specifies the number of crank angle degrees between top dead center (TDC) and the 50 % combustion point in the curve	8 degrees *
D	Duration (10% to 90% burn): Specifies the duration of the combustion on terms of crank angle between 10% combustion point and the 90% combustion point.	25 degrees *
E	Wiebe exponent	2 *
C	Wiebe constant	Calculated by model
S	Start of combustion	Calculated by model
* Recommended values for 4-stroke engines [5]		

2.3.3 Valvetrain

The Honda VFR 800 engine uses a valvetrain with chain driven dual overhead camshafts and four valves per cylinder. It uses a simple version of variable valve lift (Honda VTEC) that employs only two valves per cylinder at low engine speeds. All four valves are employed above approximate 6800 rpm and are set in motion by an electronically controlled oil spool valve. The pressurized oil actuates small slide pins which move into slots under the valve lifters allowing them to actuate the valve. In GT-Power the "ValveCamConn" object is used to model the flow through the intake exhaust valves. The model requires timing data for the valves which is entered in angle/lift array. True valve lift curves for the Honda VFR 800 are not readily available, but general timing data for intake and exhaust valve opening and closing (specified at 1 mm lift) are available in the service manual. The curves as shown in **Figure 2-5** are estimates for the entire array based on the four opening and closing times and a maximum valve lift of 8 mm. The flow rate through the valves is described as compressible flow through a restriction. The product of the experimentally determined discharge coefficient C_d and the valve curtain area A_r are used to describe the effective flow area [6]. In Chapter 6.2.3 John Heywood assumes C_d near constant, and A_r to vary with the valve lift, the GT-Power model, however, assumes A_r to be constant and varies C_d with the ratio of valve lift over valve area L_v/D_v. The maximum values for C_d are determined as in **Table 2-6**. The VTEC functionality of the valves is modeled as an orifice element, varying diameter between the valves and the intake ports. The diameter is equal to the connected intake port for engine speeds greater than 6800 rpm and equal to 0 for lower engine speeds.

Table 2-6: Discharge coefficients for intake and exhaust valve

	Size D_v	**L_v/D_v**	**Discharge coefficient C_d**
Intake valve	29 mm *	0.28	0.5 **
Exhaust valve	27.5 mm *	0.29	0.6 ***

* Values from the official Honda VFR 800/A Interceptor Service Manual

** Value extracted from [6] Figure 6-16

*** Value extracted for valve shape (a) from [6] Figure 6-18

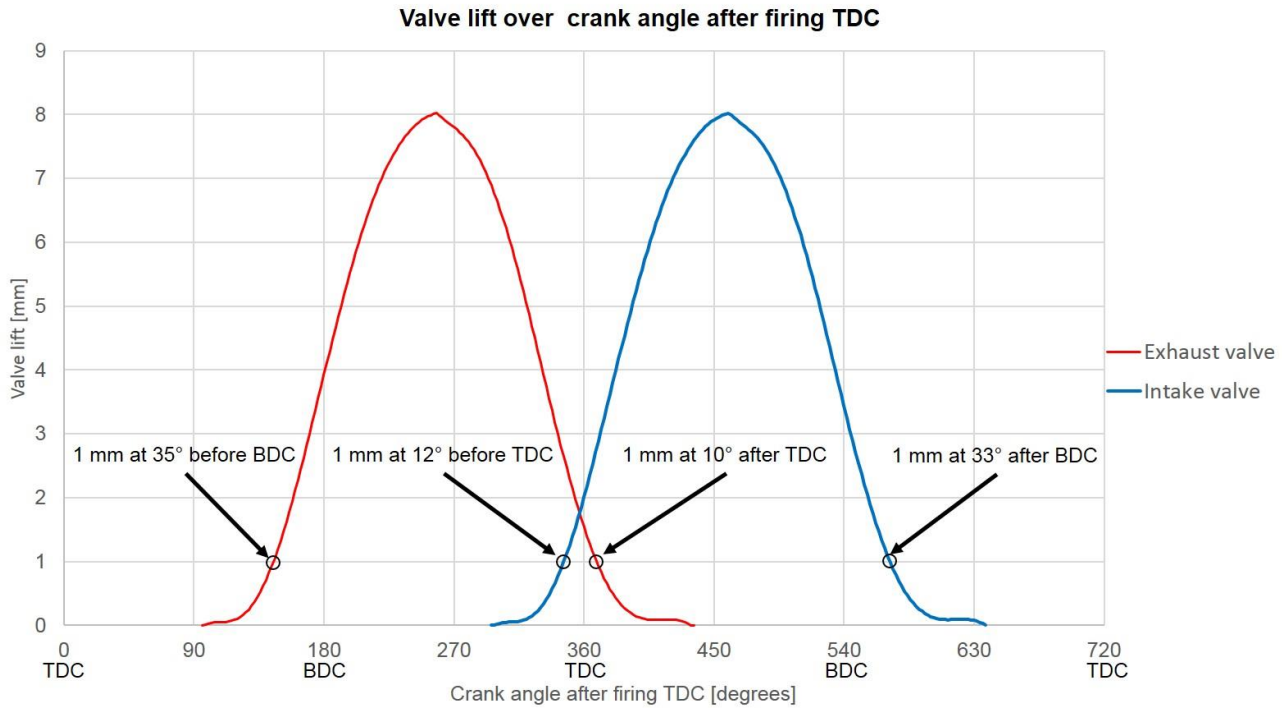

Figure 2-5: Estimated Honda VFR 800 valve lift array

2.3.4 Air Intake System

The air intake system is comprised of the intake ports, intake runners, throttle bodies, air cleaner and air inlets. All of the objects used to model these parts share the same initial fluid state as defined in **Chapter 2.3.1**. The air cleaner is represented by a single flow split object with the volume measured for the physical part. The pressure losses in the air cleaner are mostly associated with the expansion and contraction of the flow from small to large cross-sections and back. It has 2 inlet pipes, at its top plane, that connect it to the environment and 4 outlets that connect it to the individual cylinder intake runners. Each cylinder has its individual 36 mm diameter throttle body integrated in the intake runners. Modeling the throttle as a "ThrottleConn" object, the flow through the throttle for a given throttle angle is modeled in dependency of an experimentally determined discharge coefficient [6]. For this model, a simple orifice connection object is used as an alternative, and the length of the throttle body is added to the adjacent intake runner. The diameter is varied from small values up to a maximum of the throttle bore, less the throttle plate shaft area. **Table 2-7** lists the parts of the air intake represented by objects as seen in **Figure A-3**.

Table 2-7: Honda VFR 800 air intake parts

Intake system part	Characteristic size	Wall temperature estimates	Material roughness like
Primary air inlet	Length: 150 mm *	300 K	Smooth plastic
	Cross section: 1624 mm *		
Secondary air inlet	Length: 75 mm *	300 K	Smooth plastic
	Cross section: 2680 mm *		
Air cleaner	Volume: 7.7 L*	300 K	Smooth plastic
Intake runner, cylinders #1 and #3	Length: 52 mm *	300 K	Smooth plastic
	Diameter: 35 mm *		
Intake runner, cylinders #2 and #4	Length: 64 mm *	300 K	Smooth plastic
	Diameter: 35 mm *		
Throttle body (length in model added to intake ports)	Length: 25 mm *	300 K	Cast-iron
	Diameter: 36 mm *		
Intake port before split	Length: 50 mm *	300 K	Cast-iron
	Diameter: 35 mm *		
Intake port flow split	Length: 30 mm *	450 K	Cast-iron
	Volume: 28863 mm^3 *		
Intake ports after split	Length: 30 mm *	450 K	Cast-iron
	Diameter: 25 mm *		
* Values measured of the physical parts			

2.3.5 Fuel Injectors

The Honda VFR 800 engine is port injected with individual cylinder injectors inside each intake runner, just after the throttle bodies. The engine is converted to operate on E85 fuel and the fuel map is set up to operate the engine stoichiometrically throughout the entire speed-load map. E85 is a mixture of 85%

ethanol and 15% gasoline. These two fuels have a stoichiometric air-fuel ratio of 9.0 and 14.6 [6] that yields an air-fuel ratio of 9.8 for a stoichiometric mixture of E85 and air. “InjAFSeqConn” objects are used to model the fuel injectors in GT-Power. The injection timing is set to injection start at 360° before firing TDC, while a 15% fraction of the fuel is assumed to vaporize immediately upon injection.

2.3.6 Exhaust System

The exhaust system used in the UW Camaro is very different from the original system in the Honda VFR 800. As required by competition rules, a custom system is designed and built to fit the engine in the car’s engine bay, and to route the exhaust pipe under the car to the same outlet location as in the stock vehicle. The Honda Original Equipment Manufacturer (OEM) system has a 4-2-1-2 design and individual 1 ¼ inch runner pipes with a length of 500 mm from each cylinder exhaust port to the first merge. The pipes from cylinder #1 and #2 merge and those from #3 and #4 merge. After short connecting pipes merge, all exhaust merges into a single catalytic converter. A single 1 ¾ inch pipe of 400 mm length routed to a flow split which divides the exhaust flow to two individual silencers. A graphic representation of the Honda VFR 800 exhaust system can be found in **Figure 2-6** and that of the UW Camaro in **Figure 2-7**. A detailed CAD image of the UW Camaro exhaust system can be found in **Figure A-5**.

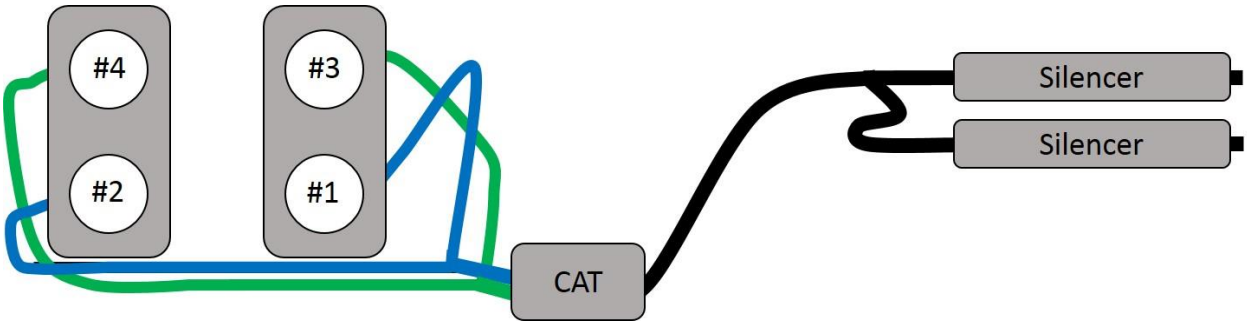

Figure 2-6: Honda VFR 800 exhaust system

The 4-2-1 exhaust system design used in the UW Camaro application has much shorter runner pipes for each cylinder. The 1 ¼ inch pipes of cylinders 2 and 4 as well as the cylinder pipes of 1 and 3 merge soon after the exhaust ports. Two separate catalytic converters follow, then the main exhaust collector. Shorter distances from the exhaust ports to the catalytic converters help to lower emissions through a quicker heat up process after engine cold start. A 1 ½ inch pipe of 3200 mm length is routed along the underbody of the

car to the silencer at the rear. Due to the length of the system the flow resistance is increased compared to the Honda OEM system.

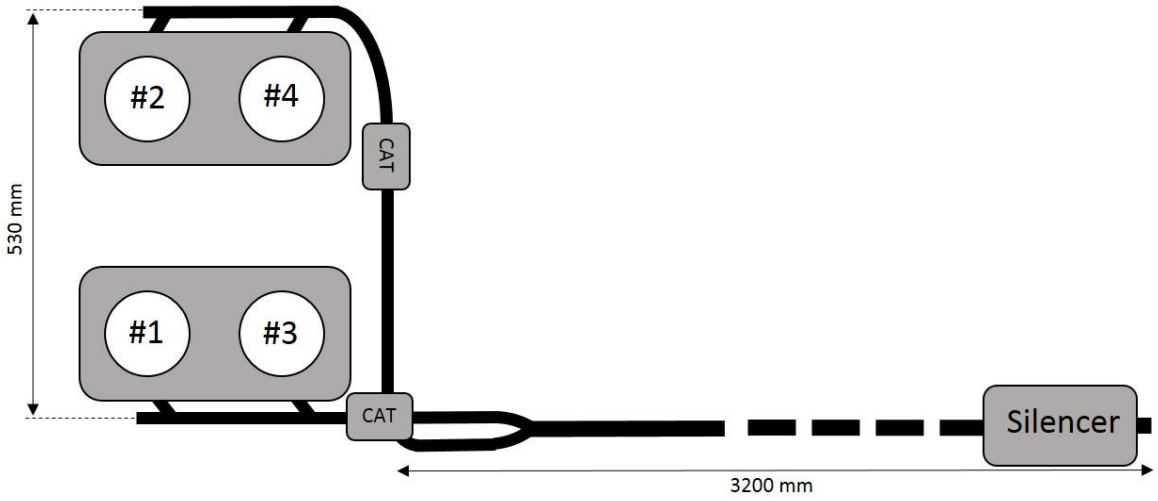

Figure 2-7: UW Camaro exhaust system

In GT-Power, the exhaust system is divided into a large number of pipe and flow split objects. **Table 2-8** lists the parts of the exhaust system and are represented as objects in GT-Power as seen in in **Figure A-4**. Many of the parts listed are represented as a chain of pipe objects and also take into account multiple bends in the routing. The entire exhaust system uses the fluid initial state “initial_exh” that has a temperature of 750 K and an absolute pressure of 1.1 bar. It is defined as the combustion products of a stoichiometric E85/air mix at chemical equilibrium. A wall temperature solver is used for all objects down the pipe from the exhaust ports. These parts undergo tremendous temperature variations with the load of the engine, because they are not actively cooled. A non-conductive orifice object is placed between the ports and the runners to isolate constant temperature parts from variable temperature parts. Parameters used for the temperature solver are listed in **Table 2-9**.

Table 2-8: UW Camaro exhaust parts

Exhaust system part	Characteristic size	Wall temperature	Material roughness like
Exhaust ports x8	Length: 40 mm *	550 K	Cast iron
	Diameter: 22 mm *		
Exhaust port merge x4	Length: 40 mm *	550 K	Cast iron
	Volume: 25876 mm^3 *		
Exhaust runners #1 / #2 / #3 / #4	Length: 100 mm / 80 mm / 80 mm / 120 mm	Wall temperature solver	steel
	Diameter: 28.7 mm *		
Exhaust runner collectors x4	Length: 40 mm *	Wall temperature solver	steel
	Volume: 38264 mm^3 *		
Exhaust header #2#4 / #1#3	Length: 1060 mm / 460 mm	Wall temperature solver	steel
	Diameter: 28.7 mm *		
Catalytic converters x2	Length: 80 mm *	Wall temperature solver	steel
	Diameter: 73 mm *		
Main exhaust collector	Length: 100 mm *	Wall temperature solver	steel
	Volume: 95662 mm^3 *		
Main exhaust pipe	Length: 3120 mm *	Wall temperature solver	steel
	Diameter: 34.9 mm *		
Silencer	Length: 120 mm *	Wall temperature solver	steel
	Diameter: 47.6 mm *		
* Values measured of the physical parts			

Table 2-9: Wall temperature solver parameters

Parameter	Value in model
Surface emissivity	0.8
Layer thickness	1.5 mm
Layer material object	Carbon steel
External convection temperature	300 K
External convection coefficient	15 W/m^2K
External radiation sink temperature	300 K
Initial wall temperature	600 K

2.3.7 Case Setup

The GT-Power case setup configuration is used to configure a number of case parameters such as engine speed, throttle (represented by variable diameter orifice connection) and intake and outlet VTEC position. A case sweep is preformed varying the engine speed form 11500 rpm to 1500 rpm in increments of 250 rpm. This is repeated for different throttle diameters varying from 33 mm to 2.5 mm, and limited to speed and throttle combination that produces a positive brake torque. The results from this 2-parameter case sweep are used to generate a BSFC map that is dependent upon engine speed (rpm) and engine load (torque).

2.4 Results of Engine Modeling

2.4.1 Comparison of Full Load Torque and Power Curves

Three different full load brake torques, and their respective brake power curves, are displayed in **Figure 2-8** and **Figure 2-10**. The red curve is based on measured data from dynamometer testing with the Honda VFR 800 motorcycle after fuel map adjustments for E85 operation. This reference curve sits between 60 to 65 Nm from the lowest measured engine speed at 3500 rpm to the highest two-valve speed at 6800 rpm. At that point VTEC switches from two-valve to four-valve operation resulting in a torque climb of 10 Nm

within 200 rpm. The torque curve peaks at 77 Nm at 8500 rpm and then falls gradually to 52 Nm at 11500 rpm. This is very close to the manufacture claims of 75 Nm at 8500 rpm. The blue curve shows results from the GT-Power mode, which, in this case is run without any exhaust system. It resembles the shape of the dynamometer measurement but at a higher torque level. The entire curve is shifted up by about 10 Nm compared to the dynamometer measurement. The lower exhaust backpressure is a possible cause for this increased brake torque output. The cyan curve displays the result of the GT-Power model, with the UW custom exhaust system. The exhaust system has a significant decreasing influence on brake torque delivery compared to the model without the exhaust system. At high engine speeds the torque falls short of the dynamometer measurement with the original motorcycle exhaust, however, at lower speeds it delivers more torque. **Figure 2-9** shows the comparison of the maximum exhaust pressure at the exhaust port collectors, for the model, with, and for the model without the exhaust system. For the UW exhaust system backpressure increased 0.5 bar at high engine speed.

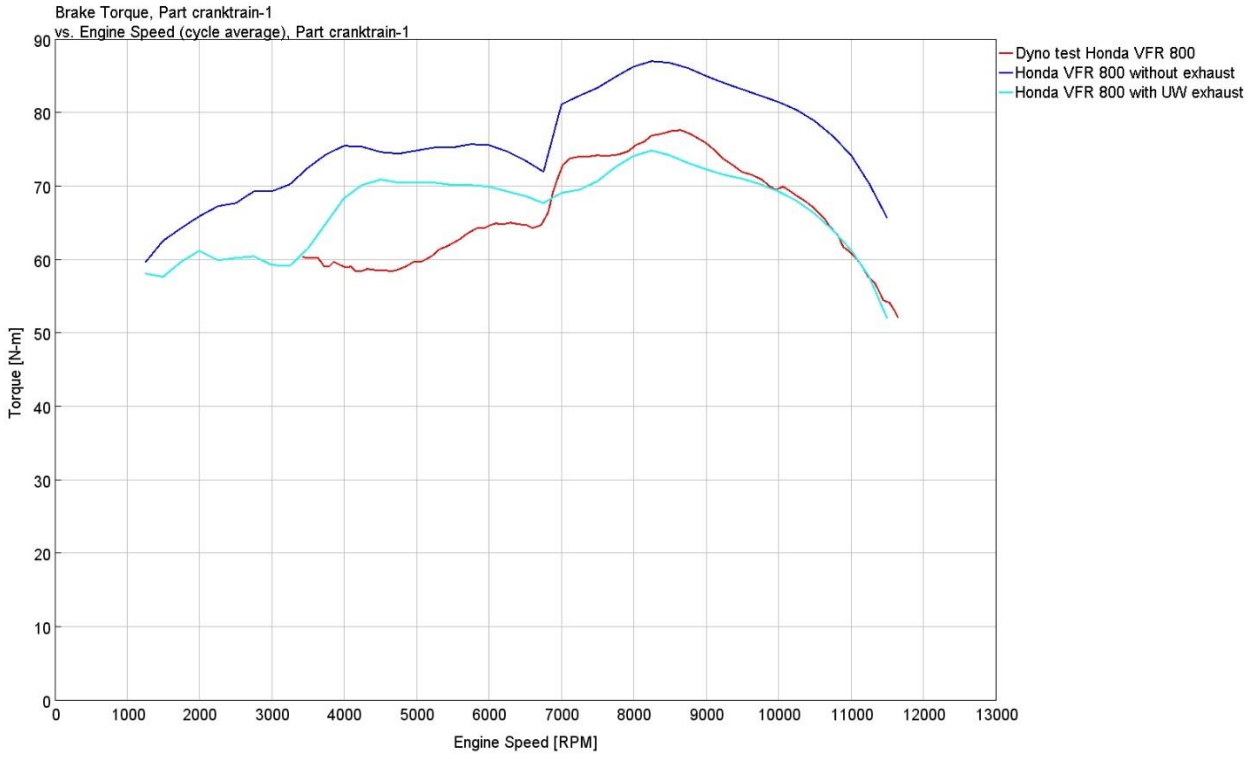

Figure 2-8: Full load torque comparison

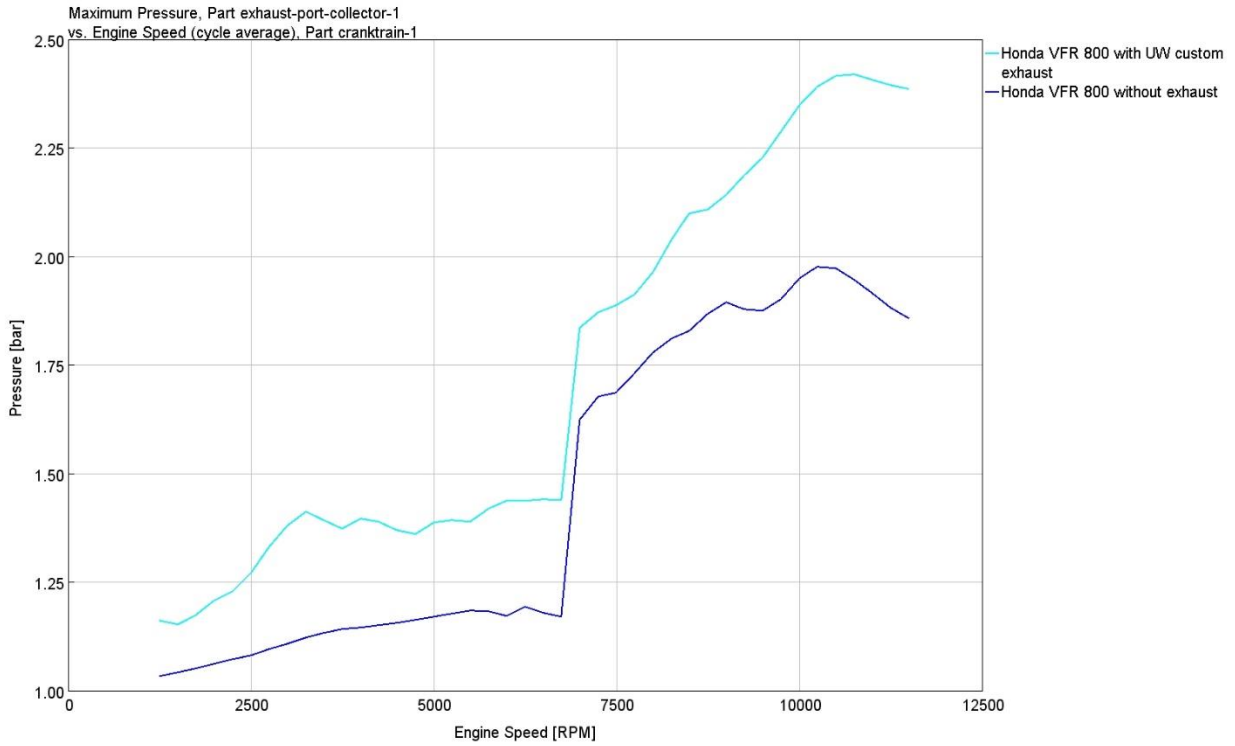

Figure 2-9: Maximum pressure inside the exhaust port collector part

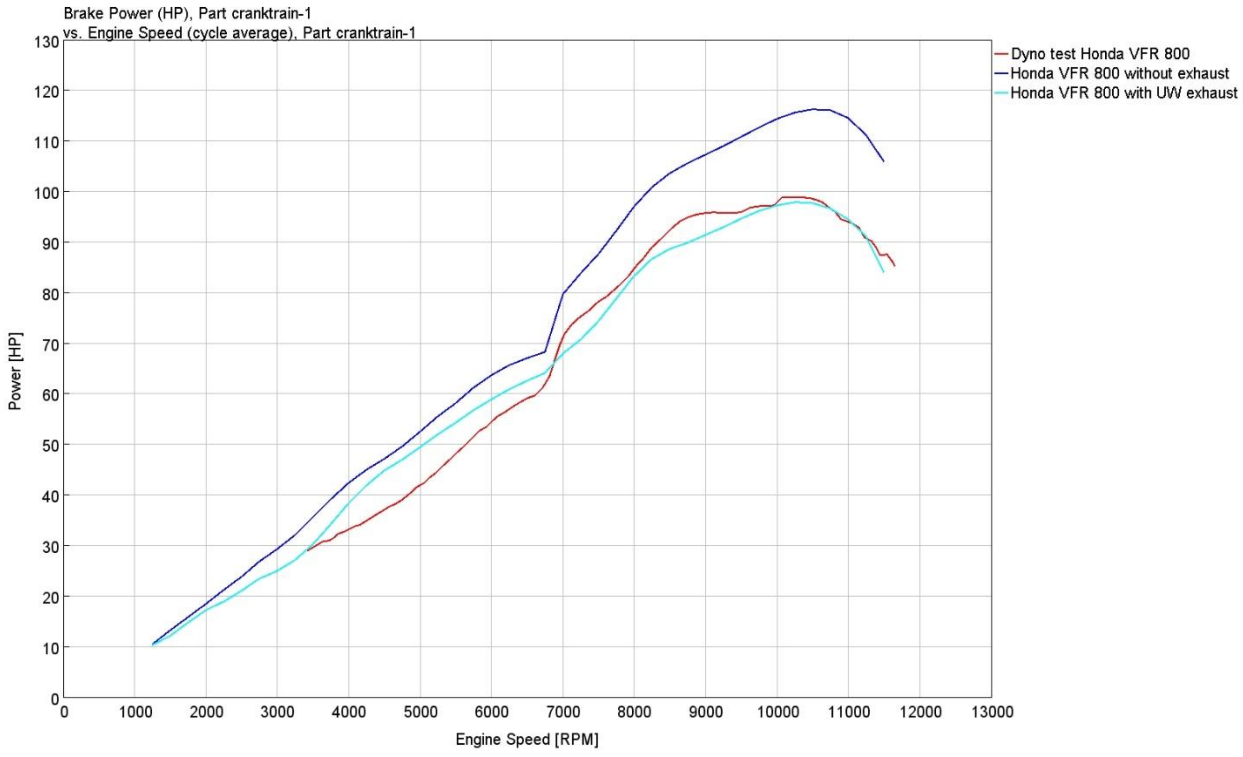

Figure 2-10: Full load power comparison

2.4.2 BSFC Map

Figure 2-11 shows the BSFC map for the GT-Power engine model with the UW custom exhaust system. It is defined in grams of E85 fuel consumed per kWh of mechanical brake energy put out by the engine and plotted over engine speed and engine load (torque). The map resembles the typical shell structure expected for a combustion engine. The lowest specific fuel consumption of 325 g/kWh is achieved in an island region between 4000 and 6000 rpm engine speed for 90% to 100% engine load. The higher heating value (HHV) of E85 fuel is 32.4 MJ/kg based on a 15% mass fraction of gasoline and an 85% mass fraction of ethanol [6]. Based on the HHV the thermal energy conversion efficiency of the engine reaches 34.3% at the best point. This best point cannot be utilized permanently, in charge sustaining mode, due to continuous torque limitations of the motor-generator. Additional graphs for 15, 20 and 25 kW engine brake power output and maximum continuous torque output by the motor-generator are plotted on top of the BSFC map. For 20 kW power a minimum specific fuel consumption of 350 g/kWh is achievable in 6th gear. This results in a 31.8% energy conversion efficiency, an 8% loss compared to the engine's best point. Lower gears result in an even lower efficiency of 30.7% for 5th gear and 29.7% for 4th gear.

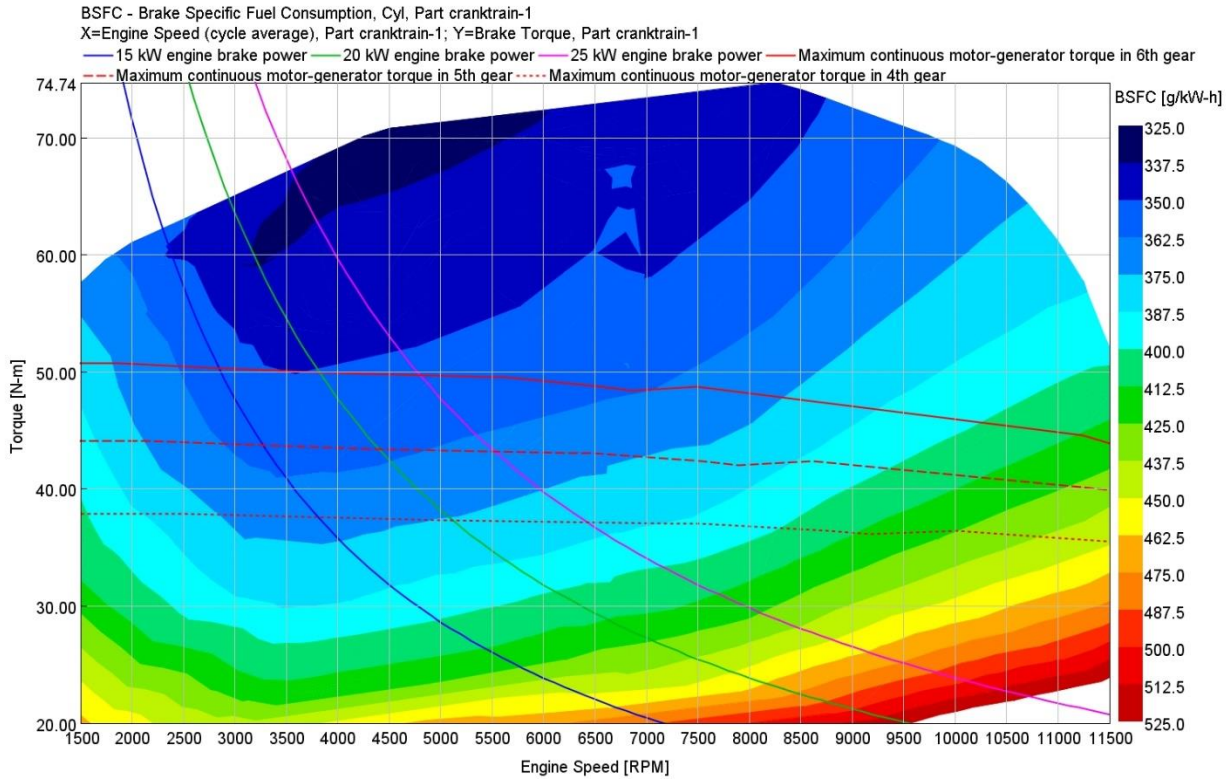

Figure 2-11: BSFC map for Honda VFR 800 engine model with UW custom exhaust

2.5 Conclusions of Engine Modeling Results

1. The engine set point with the lowest brake specific fuel consumption cannot be used permanently because of motor-generator limitations for continuous torque.
2. The best continuously usable engine set point delivers a fuel efficiency 8% lower than the best engine set point.
3. Reducing the throttle angle and thus the torque output by the engine leads to overproportional increase of brake specific fuel consumption. Consequently, it is desirable to change speed but maintain the torque output to adjust the power output of the engine if desired.

2.6 Future Work for the Generator System

The currently implemented generator system control strategy operates the engine in a stationary set point to achieve a power output of 20.4 kW limited by the continuous charge limit of the ESS. This strategy does not consider the driving loads experienced by the vehicle. The fuel efficiency of the vehicle can be improved by implementing a load following strategy of for the generator system. This strategy can be used to increase the power output of the generator system beyond 20.4 kW during charge sustaining mode, depending on the instantaneous power demand of the electric powertrain. This strategy can recharge the batteries faster and reduce the use of battery power during generator operation at low to medium driving loads. Avoiding the use of battery power during generator operation but using generator power directly for propulsion avoids losses associated with the double energy conversion from electric energy provided by the generator to chemical energy stored in the battery pack and back to electrical energy for the powertrain. Delivering electric power directly to the drive motors rather than charging the battery lowering losses associated with double energy conversion form electric to chemical and back.

Another area of possible generator system improvements is the conversion of the engine from traditional Otto cycle to Atkinson cycle. Atkinson cycle engines find increasing popularity in full hybrid electric powertrains such as the one used in the Toyota Prius. It reduces peak power and power density of the engine but improves the brake specific fuel consumption. The cycle involves an increased geometric compression ratio while reducing the fresh air charge taken in by the engine, typically by closing the intake valves late. This maintains the effective compression ratio but increases the effective expansion ratio of the

engine leading to improved thermal efficiency. For an existing engine, the geometric compression ratio can be increased by machining down the cylinder head or changing the cylinder head gaskets to thinner ones. Late closing intake valves can be implemented by designing camshafts with adjusted intake cam lobe profiles.

3 SHAFT DESIGN

3.1 Electric Powertrain

The series-TV architecture employs two independent powertrains for each rear wheel. This involves 2 sets of Emrax 268 drive motor, gearbox, Constant Velocity Joint (CVJ) and half-shafts as shown in **Figure 3-1.**

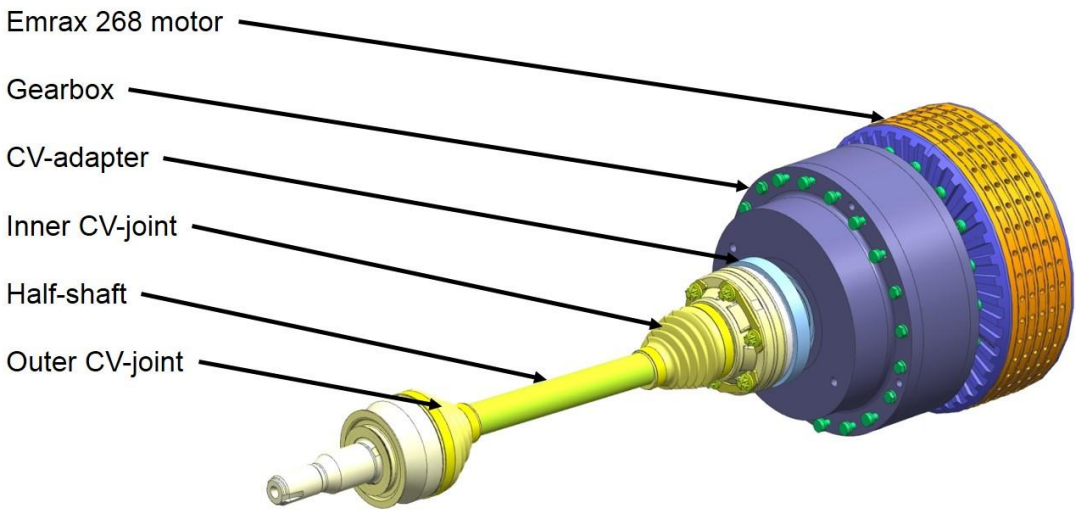

Figure 3-1: Powertrain assembly

The gearbox and half-shaft components of the powertrain are designed and manufactured by the team. The gearbox is a single speed planetary configuration with a reduction ratio of 4.2 selected to match the maximum motor speed with the desired maximum vehicle speed of 85 mph. Design details for the gearbox can be found in **Section A.1.** The gearboxes and motors are mounted to the modified rear subframe of the UW Camaro with a team-designed part not shown in the figure above. The gearboxes are filled with 1 quart of transmission fluid and vented through hoses and expansion tanks.

3.2 Strength Analysis for the CV-Adapter Part

The objective of the following analysis is to determine stress and strength of the CV-adapter part. When the this stress analysis was conducted in the middle of EcoCAR 3 Year 3, the gearboxes were already designed, manufactured and integrated, however, suspicion arose about the stress of the CV-adapter part, and its strength given the original material specifications. The original material choice is AISI 4140 steel pre-hardened to HRC 27 to 32 [7]. This material has a minimum yield strength S_y of 790 MPa, further heat treatment was not applied. Stress analysis in the following chapter will prove the strength of the original part to be insufficient and while using the original part the torque output of the motors had to be limited to 250 Nm to avoid any damage to the gear boxes. The goal of the analysis is to specify a new combination of material and heat treatment suited for the CV-adapter part and full motor torque output. If possible, changes of any geometry like increasing the part's diameter is avoided as it would require the redesign of all parts in the output half of the gearbox as highlighted in **Figure 3-2**.

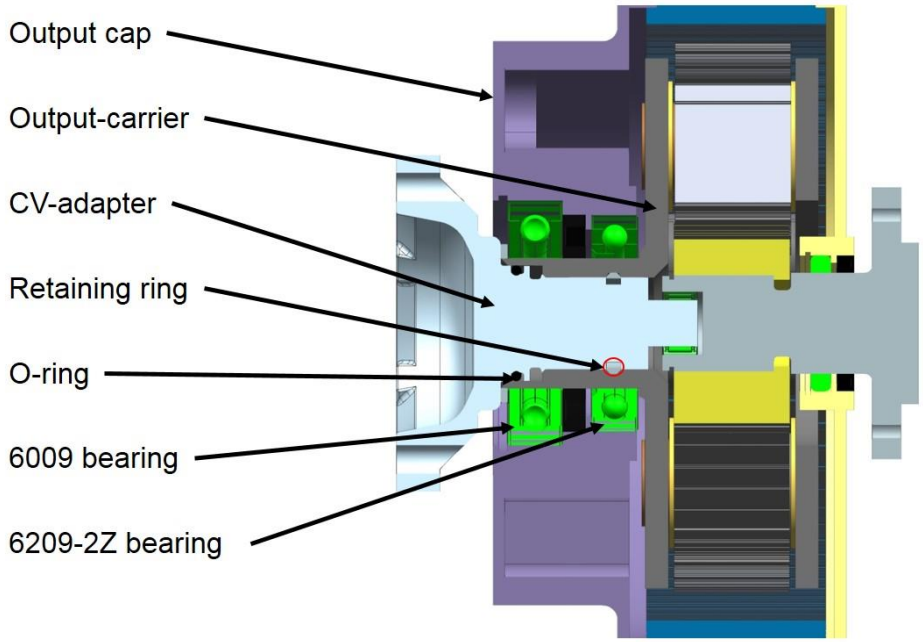

Figure 3-2: Gearbox parts affected by a possible redesign lowering the stress on the CV-adapter part

3.2.1 Critical Features

Details for the part geometry are shown in **Figure 3-3** and **Figure 3-4**. Important features from the right to the left are:

- A small diameter end section which provides support for the gearbox input shaft
- A splined section which mates to the output carrier inside the gearbox. It has a retaining ring groove to fix the CV-adapter to the output carrier in axial direction.
- A splined section transitions into a relief groove required for the spline broaching tool.
- A shoulder which is used to stop the part during assembly when it is pressed into the output carrier until the shoulder rides up against it.
- An o-ring groove to prevent transmission fluid leaks between the CV-adapter and the output carrier.

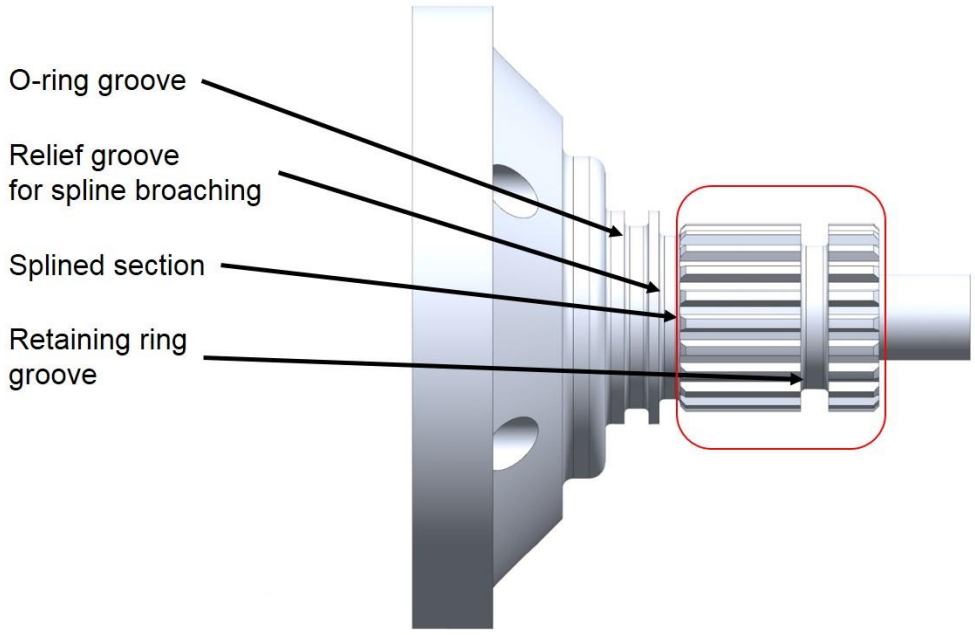

Figure 3-3: 3D representation of the CV-adapter with critical features

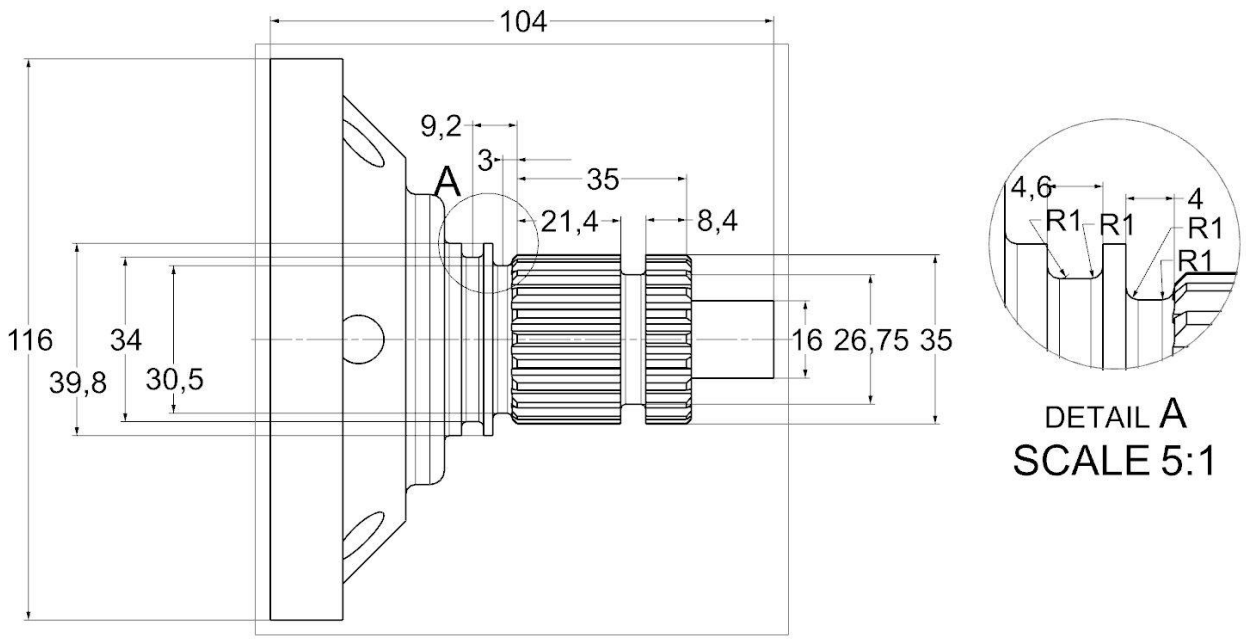

Figure 3-4: Drawing of the CV-adapter with critical dimensions in mm

3.2.2 Load Analysis

The specified peak torque output of the Emrax 268 motor is 500 Nm for a short duration at a current draw of 400 A. The battery provides a maximum of 600 A in discharge mode for a duration of 10 s. The remaining 200 A needed for both motors at full torque output is provided by the generator. According to this the maximum 500 Nm motor torque is assumed to be the maximum input torque to the gearbox. This results in a maximum 2100 Nm of torque being distributed to the CV-adapter part which is the output stub-shaft of the gearbox and the mating part to the inner CVJ. For the stress calculation, the part is assumed to be fixed at its left end and torque is applied evenly at the splined area. The retaining ring groove only receives a 28% fraction of the full torque applied to the part which means it has significantly less torsional stress than the relief groove and the o-ring groove despite its small 26.75 mm diameter. In addition to torsion a bending moment occurs in the part but axial forces are small because of the axial play in the inner CVJ and thus ignored in this analysis. The bending moment is a result of the radial bearing forces which are a result of the Z-articulation of the half-shaft and the CVJs. The forces are calculated as in **Figure 3-5**.

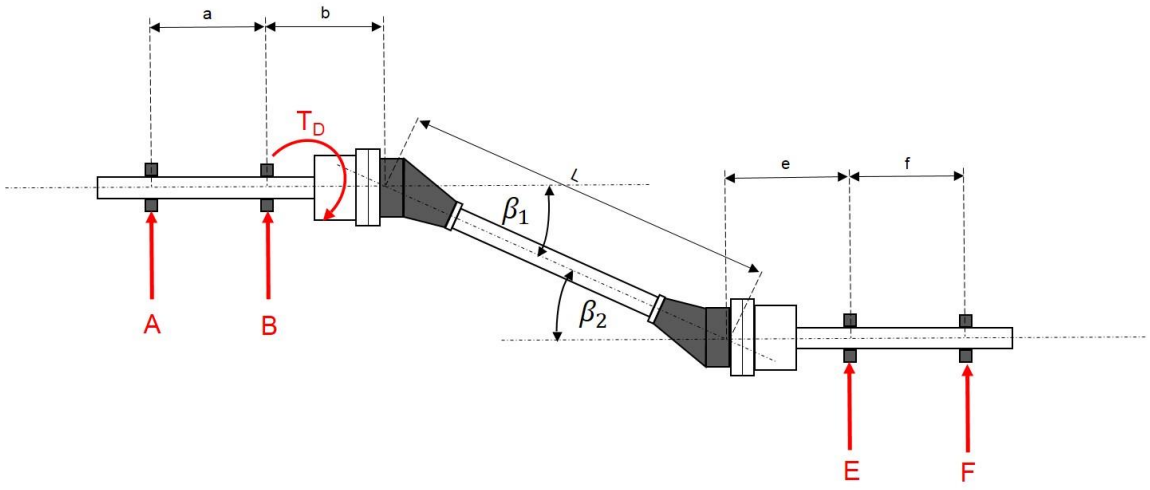

Figure 3-5: Radial bearing connection forces of Constant Velocity Joints (CVJ)

$$A = \frac{T_d}{a}\left[\tan\frac{\beta_1}{2} + \frac{b}{L}\left(\tan\frac{\beta_2}{2} - \tan\frac{\beta_1}{2}\right)\right]$$

$$B = \frac{T_d}{a}\left[\tan\frac{\beta_1}{2} + \frac{a+b}{L}\left(\tan\frac{\beta_2}{2} - \tan\frac{\beta_1}{2}\right)\right]$$

$$F = \frac{T_d}{f}\left[\tan\frac{\beta_2}{2} - \frac{e}{L}\left(\tan\frac{\beta_2}{2} - \tan\frac{\beta_1}{2}\right)\right] \quad (3.1)$$

$$E = \frac{T_d}{f}\left[\tan\frac{\beta_2}{2} - \frac{e+f}{L}\left(\tan\frac{\beta_2}{2} - \tan\frac{\beta_1}{2}\right)\right] \text{ [8]} \quad (3.2)$$

The maximum CVJ angel for the UW Camaro is approximately 15° under any driving condition and with the angles β_1 and β_2 assumed to be equal the equations (3.1) and (3.2) can be written as:

$$E = -F = \frac{T_d}{f} * \tan\frac{\beta}{2} \text{ [8]} \quad (3.3)$$

For the CV-adapter the forces E and F are not bearing forces as assumes in **Figure 3-5** but a reaction force in the splined area. The reaction force in the splined area is assumed to be linearly distributed as in **Figure 3-6 (a),** ignoring the retaining ring groove. The combined forces E and F are distanced 1/6 of the splines

length (sp) from the left and the right end of the splines respectively. This leads to f being 2/3 of the splined length or 23.33 mm and using equation (3.1):

$$E = -F = 11849 \text{ N}$$

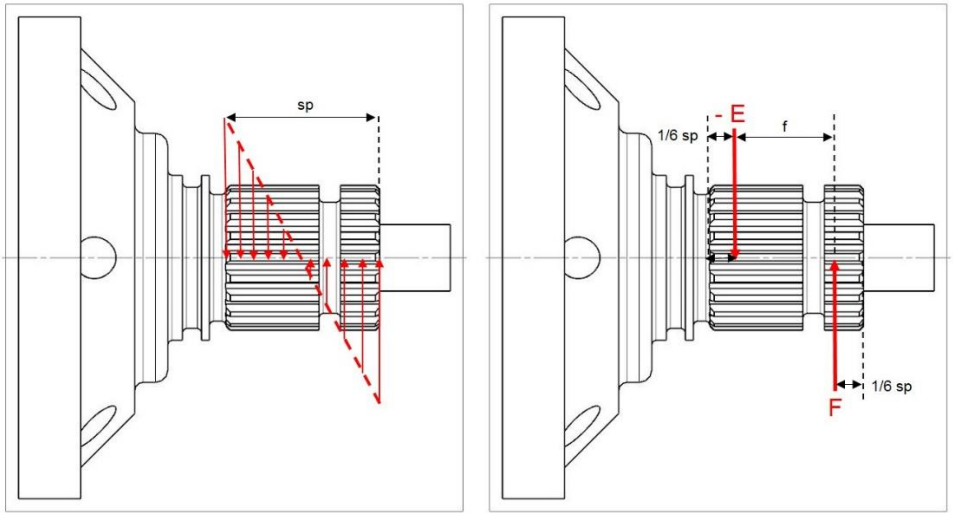

Figure 3-6: CV-adapter reaction forces

The bending moments are significant in both, the relief groove and the o-ring groove as in **Figure 3-7.**

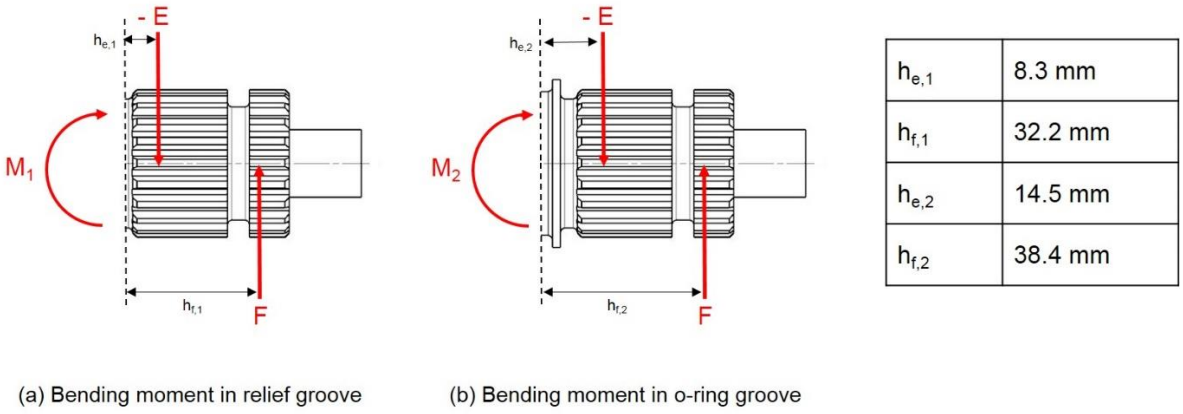

$h_{e,1}$	8.3 mm
$h_{f,1}$	32.2 mm
$h_{e,2}$	14.5 mm
$h_{f,2}$	38.4 mm

Figure 3-7: CV-adapter bending moments

For the bending moments the geometry of the CV-adapter part in Figure 3-7 yields:

$$M_1 = M_2 = 276\ \text{Nm}$$

3.2.3 Static Stress Analysis

The stress in the critical features of the CV-adapter are subject to stress concentration due to notch effects. To determine static stress concentration factors, both grooves are treated as U-shaped grooves. The geometry parameters and concertation factors are as in **Table 3-1.**

Table 3-1: Groove geometry and stress concentration factors **[9]**

Variable	Definition	Relief groove (index 1)	O-ring groove (index 2)
d	Smaller diameter at the groove	30.5 mm	34 mm
D	Larger diameter at the groove	35 mm	39.8 mm
a	Length of the groove	4 mm	4.6 mm
r	Radius of the groove	1 mm	1 mm
t	Depth of the groove	2.25 mm	2.9 mm
a/t	Groove length/Groove depth	1.78	1.59
r/t	Groove radius/Groove depth	0.44	0.34
a/r	Groove length/Groove radius	4	4.6
$\boldsymbol{K_{ts}}$	**Torsion stress concentration factor**	**2**	**2**
r/d	Groove radius/Small diameter	0.033	0.029
D/d	Large diameter/Small diameter	1.15	1.17
$\boldsymbol{K_t}$	**Bending stress concentration factor**	**3.5**	**3.75**

The maximum static shear stress resulting from torsion is given by:

$$\tau_{max} = K_{ts} * \frac{T_d * r}{J},\ \text{with}\ J = \frac{\pi}{32} * d^4 \qquad (3.4)$$

The maximum static stress resulting from bending is given by:

$$\sigma_{max} = K_t * \frac{M*r}{I}, \text{ with } I = \frac{\pi}{64} * d^4 \tag{3.5}$$

To consider the possibility of first cycle failure in the first load cycle the von Mises maximum stress is calculated and compared to the yield strength of the material:

$$\sigma'_{max} = \sqrt{{\sigma_{max}}^2 + 3(\tau_{max})^2} \tag{3.6}$$

For the relief groove and o-ring groove the von Mises maximum stress yields:

$$\sigma'_{max,1} = 1351 \text{ MPa}$$

$$\sigma'_{max,2} = 612 \text{ MPa}$$

The contribution of the bending stress to the von Mises equivalent stress is very small. The torsional stress alone produces an equivalent stress of 1306 MPa for the relief groove. The relief groove is the governing feature of the part in terms of static stress. The maximum von Mises stress at this feature is used to select an appropriate material and specify hardness requirements for the part. Requiring a factor of safety for first cycle failure n_y of 1.5 leads to a minimum yield strength S_y of 2027 MPa at the surface. As expected the originally selected material in its pre-hardened condition (S_y of 790 MPa) is by far not sufficiently for the part.

3.2.4 Material Selection and Case Hardening

For torsion and bending loads the stress inside the part is highest at the surface and decreases linearly to zero at the neutral axis, which is the center line for round shafts [10]. This rule is used to determine the stress inside the part at a certain distance from the surface. Using a hardness-strength conversion table for different steel, a minimum hardness requirement can be assigned to the stress at a certain distance from the surface as shown in **Table 3-2**. AISI 4140 and 4340 steel are considered possible choices because of

their exceptional strength, good hardenability, and the availability to purchase small quantities needed by the UW EcoCAR team.

To compare the minimum hardness required at a certain distance from the surface, hardenability curves for different materials are used to determine the suitability of a material. 4140 steel and 4340 steel rod can both be purchased in normalized condition with HRC 27 minimum. Assuming the core hardness of the material remains on this level, a case depth minimum of 9 mm must be achieved for 4140 steel and 9 mm for 4340 steel respectively. Hardenability data for 4140 and 4340 steel can be found in **Table 3-3**. The surface hardness requirement for 4140 steel slightly exceeded the hardenability. Consequently 4340 steel is a better choice for the CV-adapter part.

Table 3-2: Strength requirement and hardness for SEA/AISI 4140 and 4340 steel grades

Radius [mm]	Distance from surface [mm]	Desired yield strength [MPa]	Minimum hardness 4140 steel [HRC] *	Minimum hardness 4340 steel [HRC]
15.25	0	2027	Not possible	58 **
14.25	1	1894	60 *	54 **
13.25	2	1761	57 *	51 **
12.25	3	1628	53 *	49.5 **
11.25	4	1495	50 *	48 **
10.25	5	1362	47 *	46
9.25	6	1229	40 *	43**
8.25	7	1096	36 *	39
7.25	8	964	29 *	30**
6.25	9	831	27 *	27
5.25	10	698		
4.25	11	565		
3.25	12	432		
2.25	13	299		
1.25	14	166		
0.25	15	33		

Hardness data source: [11]

* Converted from HB to HRC using: [12]

** Values are linear interpolations between neighboring values

Table 3-3: Hardenability of 4140 and 4340 steel

	SAE/AISI 4140H		SAE/AISI 4340H	
Distance from quenched end [mm]	Maximum Hardness [HRC]	Minimum Hardness [HRC]	Maximum Hardness [HRC]	Minimum Hardness [HRC]
1.5	60	53	60	53
3	60	52	60	53
5	60	52	60	53
7	59	51	60	53
9	59	50	60	53
11	58	48	60	53
13	57	46	60	53
15	57	43	60	53
20	55	38	60	52
25	53	35	59	51
30	51	33	58	50
35	49	32	58	49
40	48	32	57	47
45	46	31	57	46
50	45	30	57	45
Data source: [13]				

3.2.5 Fatigue Life

The load on the part can be described as spectrum loading with occasional overloading during high motor torque demands by the driver, and a manifold of smaller cycles due to bending and changing lower torque demands. For the assessment of the fatigue life of the part the torque load is assumed to be alternating between the maximum propulsion torque and the maximum regenerative breaking torque. The bending load is alternating and sinusoidal but small compared to the torque load. It has a linear dependency on the torque load as stated in equation (3.3). High motor torque outputs only occur under full acceleration therefore the bending load is significantly diminished most of the time (the maximum vehicle speed is limited to 85 mph requiring less than full torque). Also, bending load depends on the CVJ angle as stated in equation (3.1), which is close to 0° most of the time in the UW vehicle. In conclusion, the bending load is ignored for fatigue analysis. Stress concentration factors for fatigue in notched parts differ from the stress concentration factors in static stress. The effect of notches in fatigue strength is determined by comparison of Stress-Cycle (S-N) curves of notched and unnotched parts. A new stress concentration factor K_f is introduced as follows [14]:

$$K_f = \frac{Fatigue\ limit\ unnotched}{Fatigue\ limit\ notched} \tag{3.7}$$

K_f is always smaller than K_t (Stress concentration factors for static load). Notch fatigue data is reported in the form of sensitivity factors q, where [8]

$$q = \frac{K_f - 1}{K_t - 1} \tag{3.8}$$

Lower strength materials are less affected by notch sensitivity due to their capacity for the deformation and crack tip blunting that relieves stress. [14]. Also, q decreases with smaller notch radii because K_f increases more slowly than K_t. The dependency of q and K_f is as follows [14]:

$$K_f = 1 + q(K_t - 1) \tag{3.9}$$

The case-hardened steel used for the CV-adapter with ultimate tensile strength S_{ut} = 2200 MPa minimum yields a value if q = 0.95 [15]. As stated in **Table 3-1** and K_{ts} is 2 which yields 1.95 for K_{fs} which is only a marginal difference due to the high hardness of the material used.

Given the loads and fatigue stress concentration factor of the part, the effective stresses can be calculated analog to equation (3.2) and (4.5). The results are as in **Table 3-4**.

Table 3-4: Fatigue stress CV-adapter

Load/stress	Value	Explanation
T_{max}	2100 Nm	Maximum propulsion torque
T_{min}	-252 Nm	Maximum regenerative breaking torque
τ_{max}	735 MPa	Maximum torsional shear stress
τ_{min}	-88 MPa	Minimum torsional shear stress
τ_a	478 MPa	Amplitude of torsional shear stress
τ_m	323 MPa	Mean torsional shear stress
σ'_a	828 MPa	Von Mises equivalent stress amplitude
σ'_m	560 MPa	Von Mises equivalent mean stress

The endurance limit S'_e for most steel is about half of its ultimate tensile strength S_{ut} [16]. This relationship only holds up to a hardness of approximately 40 HRC. For values above 40 HRC the scatter for individual test specimens used to obtain S-N curves becomes too great. The endurance limit for high-strength steel is extremely sensitive to surface condition, residual stress, and presence of inclusions acting as stress concentration [14]. The endurance limit for the case hardened 4340 steel can assumed to be S'_e = 700 MPa [15]. In the laboratory, the endurance limit for different materials is tested with an unnotched rotating-beam specimen. The design endurance limit S_e of a part is significantly lower than the material endurance limit tested under lab conditions. Factors known as Marin factors are used to adjust the endurance limit. The equation for S_e can be written as:

$$S_e = k_a k_b k_c k_d k_e k_f S'_e \text{ [15]} \quad (3.10)$$

- The surface factor k_a is a correction factor for the surface roughness of a design part and can be expressed as:

$$k_a = aS_{ut}^b \text{ [15]} \tag{3.11}$$

- The size factor k_b for torsion can be expressed as:

$$k_b = 1.24d^{-0.107} \text{ for } 2.79 \leq d \leq 51 \text{ mm [15]} \tag{3.12}$$

- The loading factor k_c reduces the endurance limit for torsion and axial load compared to bending load.
- The temperature factor k_d describes the lowered fatigue endurance limit at higher operating temperature.
- Material endurance strength data is reported as mean values of scattered data with a standard deviation of less than 8 percent [15]. The reliability modification factor k_e accounts for this and can be expressed as:

$$k_e = 1 - 0.08z_a \text{ [15]} \tag{3.13}$$

- Miscellaneous effects like corrosion, electrolytic plating, metal spraying, etc. are summarized in the factor k_f. For the CV-adapter part the individual factors can be obtained as follows:

Table 3-5: Marin factors for the CV-adapter part

Marin factor	Value for CV-adapter	Explanation
k_a	0.60	a = 4.51 and b = -0.085 for machine finished parts
k_b	0.86	d = 30.5 mm
k_c	0.59	Torsional loading
k_d	1	Ambient temperature assumed
k_e	0.90	90% reliability assumed, z_a = 1.288
k_f	1	No miscellaneous effects assumed

As a result the design endurance limit S_e of the CV-adapter is as low as 192 MPa. The fatigue factor of safety in based on infinite life of the part can be expressed based on the modified Goodman criterion, which can be expressed as:

$$\frac{1}{n_f} = \frac{\sigma'_a}{S_e} + \frac{\sigma'_m}{S_{ut}} \text{ [15]} \tag{3.14}$$

For the CV-adapter the equation yields n_f = 0.30 which means the part clearly has a finite life time. To predict the limited life time of the part for a number of cycles N between 10^3 and 10^6 the following equation can be used:

$$N = \left(\frac{\sigma_{rev}}{a}\right)^{\frac{1}{b}} \text{ with } a = \frac{(fS_{ut})^2}{S_e} \text{ and } b = -\frac{1}{3}\log\left(\frac{fS_{ut}}{S_e}\right) \text{ [15]} \tag{3.15}$$

This equation only applies to completely revered stress σ_{rev} as S-N diagrams are only applicable for completely reversed stress. For other cases an equivalent complete reversed stress must be calculated using substituting S_e with σ_{rev} using equation (3.14).

$$\sigma_{rev} = \frac{\sigma'_a}{1-\frac{\sigma'_m}{S_{ut}}} \text{ [15]} \tag{3.16}$$

Equation (3.15) also contains a factor f. It is used to approximate the fatigue strength of a steel at 10^3 cycles.

$$f = \frac{\sigma'_F}{S_{ut}}(2 \cdot 10^3)^b \text{ with } \sigma'_F = S_{ut} + 345 \text{ MPa, and } b = \frac{\log(\sigma'_F/S'_e)}{\log(2 \cdot 10^6)} \text{ [15]} \qquad (3.17)$$

Plugging in the numbers from the tables and results above yields:

$$N = 1600$$

3.2.6 Finite Element Analysis (FEA)

For comparison, the stress for CV-adapter part was analyzed in Siemens NX Nastran. The part was meshed with a 3D tetrahedral elements of 1 mm size. The element size was decreased in consecutive FEA runs on the part until the highest stresses in the solution converged. The part is fixed at its left end in **Figure 3-8** and a 2100 Nm torque load is applied in the splined section where the spline geometry is ignored for this case because the focus of the analysis is on the grooved sections of the part. The results confirm the relief groove to be the most stressed feature of the part. A maximum stress of 1059 MPa in the relief groove for pure torsion is 19% lower than the results obtained by hand calculation (1306 MPa). Possible reasons for the lower stress shown in FEA are:

- The o-ring groove acts as a shoulder relief groove on the spline relief groove lowering the maximum stress experienced by the part [15] This stress relief effect is not quantifiable readily available text book style equations.
- The stress concentration factor for torsional loading in section 3.2.3 is overestimated. The used stress concentration factor charts only cover U-shape grooves for in the range of geometry factors of the CV-adapter part. The actual groove geometry can be described as a flat bottom groove or two shoulder fillets. For comparison, a chart for shoulder fillets yields a stress concentration of K_{ts} = 1.75.

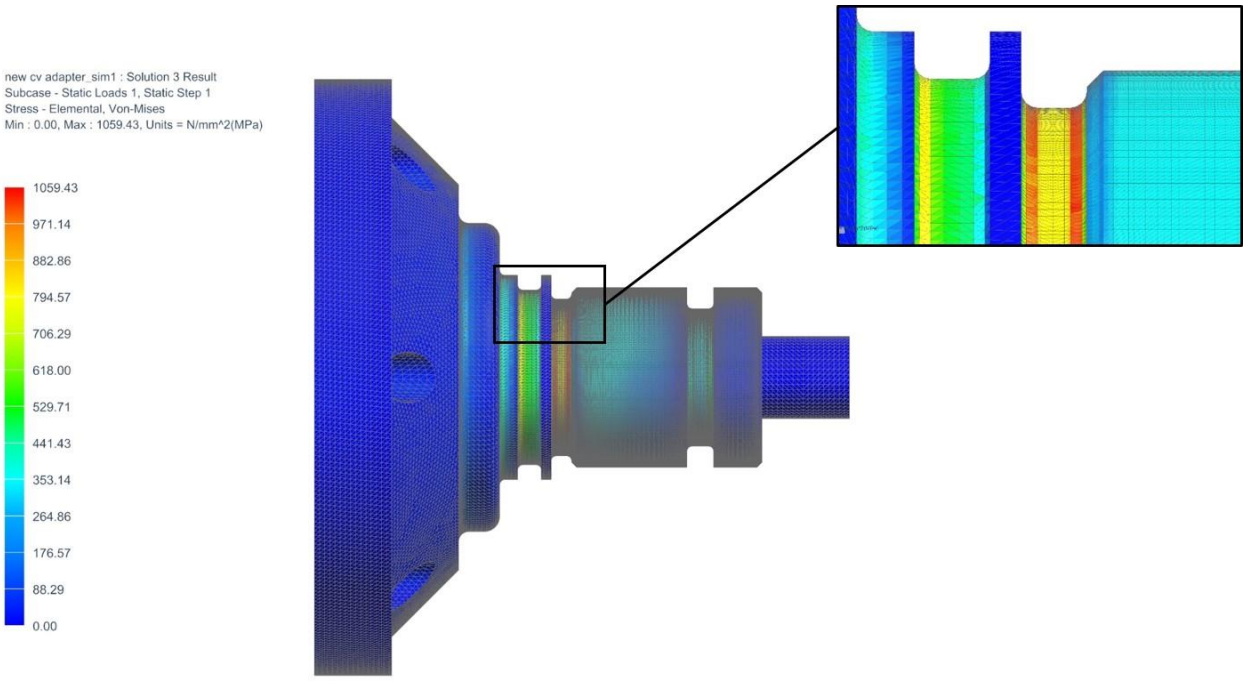

Figure 3-8: Results of CV-adapter finite element analysis in NX Nastran

For comparison, the stress results from FEA are used for the same equation in Chapter 3.2.5 to determine the fatigue life of the part for the lower stress. The same material properties and case hardening are assumed. The number of cycles is as follows:

$$N = 6280$$

3.3 Conclusions of Shaft Strength Analysis

1. The CV-adapter part can be significantly strengthened by selecting 4340 steel for use, and by applying case hardening as specified in **chapter 3.2.4**.
2. Fatigue analysis shows the part is prone to fail after a number of cycles that easily occur in the lifetime of a production car but the lifetime is long enough for Year 4 of EcoCAR 3.
3. The static and fatigue strength of the part with improved material and heat-treatment is sufficient to raise the torque limits applied to prevent gearbox failure with the original CV-adapter part.
4. Redesigning the output half of the gearbox can be avoided.

3.4 Future Work for the Gearboxes

With only one year left in the EcoCAR 3 competition no major design changes are planned for the gearboxes beyond implementation of the improved CV-adapter part. The new parts will enable the gearboxes to meet all team and competition goals in dynamic competition events. However, reduction of noise created by the gearboxes is an area of possible improvement without major structural changes. The design uses straight-cut gears that lead to high noise emissions reducing consumer appeal of the vehicle, a scored section of the EcoCAR competition. The noise emissions of the gearboxes can be reduced by implementing an enclosure using noise canceling materials.

4 SUSPENSION MODIFICATIONS

4.1 Stock Vehicle and UW Vehicle Suspension

The hybridization of the Chevrolet Camaro results in a significant change in total vehicle mass and mass distribution. This greatly affects the vibrational behavior, ground clearance and handling of the vehicle. Suspension modification is required to accommodate these affects. This chapter describes the design of new rear suspension coil springs which help to restore the ground clearance and the vibrational behavior of the vehicle.

4.1.1 Ride Height

The ride height of the vehicle is measured to determine the difference between the ride height prior to suspension modifications, and the desired ride height equal to the original ride height. The ride height of the vehicle is measured against the body of the vehicle and defined as P and R as in **Figure 4-1**:

- P height: The vertical distance from the ground to the top of the wheel opening through the center of the front wheel.
- R height: The vertical distance from the ground to the top of the wheel opening through the center of the rear wheel.

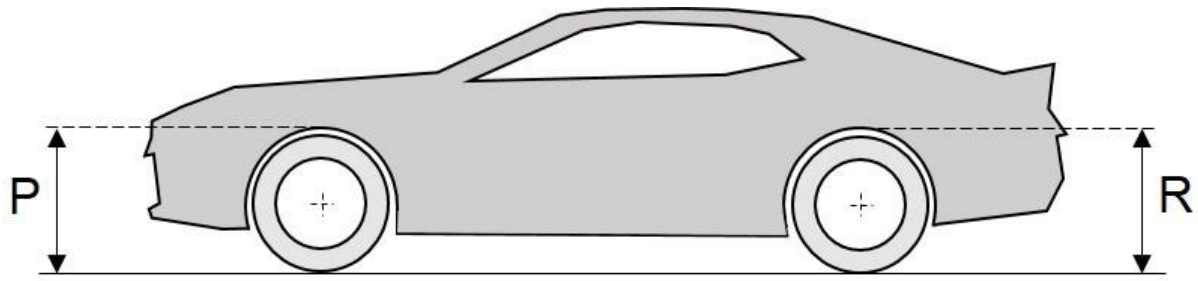

Figure 4-1: Measuring the ride height

To measure the P and R heights the following procedure is followed:

1. The tire pressure is set to specifications shown on the certification label.
2. The fuel tank is filled all the way or extra weight is used to simulate a full tank.
3. The passenger and rear compartment are empty except for a spare tire.

4. The vehicle is on a flat and level surface.
5. The vehicle is checked for aftermarket accessories or modifications possibly affecting the ride height (such as larger or smaller than production wheels and tires).
6. The bumper is pushed down a minimum of 25 mm and released a total of three times.
7. The height is measured and recorded as defined above.
8. The bumper is pulled up a minimum of 25 mm and released a total of three times.
9. The height is measured and recorded as defined above.
10. For the true height, the average of both measurements is taken.

4.1.2 Data Comparison

The vehicle's weight was measured independently at all 4 wheels with a corner scale kit. Results for mass and ride height can be found in **Table 4-1**. The total vehicle mass is increased by 190 kg compared to the stock vehicle; an increase of 12.3%. The mass is added exclusively to the rear of the vehicle because large added components like the ESS and electric powertrain are located here. As a result, the ride height is lowered by approximately 18 mm which puts it out of the OEM's tolerance filed for the stock vehicle. The front of the vehicle has a slightly reduced mass and a ride height well within the OEM's tolerance field.

Table 4-1: Mass and suspension data

	Stock vehicle with 3.6L V6 engine	UW EcoCAR 3 Year 3 vehicle (prior to suspension modifications)
Front ride height (P)	728±12 mm *	735 mm **
Rear ride height (R)	728±12 mm *	710 mm **
Curb mass, total (m_t)	1550 kg ***	1740 kg (+12.3%) ***
Curb mass, front axle (m_p)	810 kg ***	791 kg (-2.3%) ***
Curb mass, rear axle (m_r)	740 kg ***	949 kg (+28.2%) ***
Tire size	P245/50 R18 (front and rear)	
* Data given by General Motors (GM) ** Measured by UW with rear coil spring part number 23341853 Code AAZ6 *** Measured by UW with Longacre Accuset II Scale Kit		

The lowered rear ride height also has consequences for the ground clearance of the vehicle which for the EcoCAR competition must maintain a minimum of 4.75 inches (120.65 mm) for any of the sprung components of the vehicle. The UW EcoCAR 3 Year 3 vehicle undercuts the value by .5 inches (12.7 mm) prior to suspension modifications. This and the changed rear ride frequency (natural frequency of the sprung mass in the rear of the vehicle) are reasons to redesign the rear coil spring to match the stock rear ride frequency and ride height. The front of the suspension does not require any changes since the front mass changed only by 2.3% and the ride height is well within the OEM's tolerance.

4.1.3 Rear Suspension Model

The vehicle's rear suspension is a multi-link configuration with 5 control links. For this analysis all control links are ignored, except the lower control link as shown in **Figure 4-2** which seats the coil spring at its lower end and also mounts to the lower end of the damper. The upper ends of the spring and damper are attached to the car body. The wheel and coil spring have a motion ratio (r) defined by the lengths a and b. The coil spring (rate k_s) and is offset from the damper (damper rate d_d) at the lower control link. The tire also contributes a spring rate (k_t) and damper rate (d_t) to the suspension.

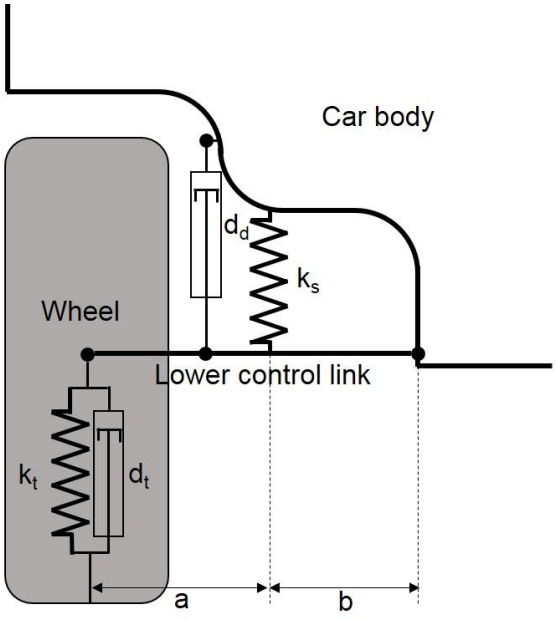

Figure 4-2: Simplified Camaro rear suspension

4.2 Calculations for New Coil Springs

A further simplified suspension model is used to calculate the parameters for new coil springs. This model is known as the quarter car suspension model. The damping ratio for passenger cars dampers in the range of 0.2 to 0.4. Given the typical range of coil spring rate and tire spring rate, the damping has little influence on the natural frequency of the sprung and unsprung mass [17]. Consequently, the dampers are ignored except the stiffness which the damper contributes to the ride rate. The masses in **Figure 4-3** are:

- Half of the rear axle unsprung mass ($m_{r,u}$) which contains the wheel and a portion of all suspension links, the spring, the damper and the drive axles.
- Half of the rear axle sprung mass ($m_{r,s}$) which is the difference between the rear curb mass (m_r) and the rear axle unsprung mass ($m_{r,u}$).

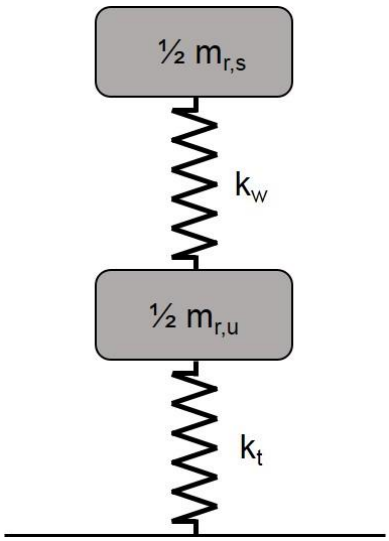

Figure 4-3: Simplified quarter car model

4.2.1 Stock Rear Ride Rate and Ride Frequency

Derived from the quarter car model the ride rate (k_r) can be calculated from the wheel rate (k_w) and tire rate (k_t) as follows:

$$\frac{1}{k_r} = \frac{1}{k_w} + \frac{1}{k_t} \tag{4.1}$$

The wheel rate (k_w) is comprised of the coil spring rate (k_s), the bushing rate (k_b) and the damper rate (k_d). For the spring rate, a motion ratio (r) has to be taken into account whereas the bushing and damper rate are directly referenced to the wheel center.

$$k_w = \frac{k_{s,stock}}{r^2} + k_d + k_b \tag{4.2}$$

The stock rear suspension natural frequency can be calculated from the stock rear ride rate and the stock rear sprung mass. The frequency target includes a fraction of the mass of two front passages (m_{2P}) to optimize the suspension behavior for a vehicle with an average number of passenger.

$$f_n = \frac{1}{2\pi}\sqrt{\frac{k_r}{m_{r,s}+m_{2p}}}\text{ , } k_r \text{ in N/m} \tag{4.3}$$

Table 4-2 contains additional parameters and results for the equations above.

Table 4-2: Suspension parameters and ride rate

Parameters	
Damper spring rate (k_d)	1 N/mm *
Bushing spring rate (k_b)	7 N/mm *
Tire spring rate (k_t)	245 N/mm *
Stock coil spring rate ($k_{s,stock}$)	85 N/mm *
Wheel to spring motion ratio (r)	1.92 *
Unsprung mass, rear axle ($m_{r,u}$)	108 kg *
Added mass for 2 passengers, rear axle (m_{2P})	73 kg *
Results	
Stock wheel rate (k_w)	31.06 N/mm
Stock ride rate (k_r)	27.56 N/mm
Rear suspension natural frequency, sprung mass (f_n)	1.41 Hz
* Data given by GM	

4.2.2 New Spring Rate and Free Length

Goal of the new spring ride rate is to match the stock ride frequency with the increased rear curb mass of the vehicle assuming the bushing, tire and damper rate are all the same as before. The new desired ride rate can be extracted from equation (4.3) which leads to a new desired wheel rate through equation (4.1). The new wheel rate allows to calculate the new coil spring rate ($k_{s,new}$) from equation (4.2). To recover the stock ride height of the vehicle a new coil spring length is determined. The stock spring load ($F_{s,stock}$) is calculated from the stock coil spring's free length ($l_{0,stock}$) and compressed length (l_1) which is measured at curb loading.

$$F_{s,stock} = \left(l_{0,stock} - l_1\right) \cdot k_{s,stock} \tag{4.4}$$

The new spring load is calculated from the difference of the UW EcoCAR 3 Year 3 vehicle prior to suspension modifications ($R_{current}$) and the stock ride height ($R_{desired}$).

$$F_{s,new} = \frac{R_{desired} - R_{current}}{r} \cdot k_{s,stock} + F_{s,stock} \tag{4.5}$$

The new spring free length is calculated under the assumption the new spring must compress to the same length as the stock spring did in the unified vehicle, now with the new spring load and rate.

$$l_{0,new} = \frac{F_{s,new}}{k_{s,new}} + l_1 \tag{4.6}$$

Table 4-3 provides the remaining parameters and summarizes the results of the spring calculations.

Table 4-3: Spring rates and lengths

Parameters	
Stock vehicle rear spring free length ($l_{0,stock}$)	325 mm **
Stock vehicle rear spring compressed length (l_1)	251.1 mm *
Results	
Stock spring load ($F_{s,stock}$)	6281.5 N
New spring load ($F_{s,new}$)	7452.8 N
New spring rate ($k_{s,new}$)	124.9 N/mm
New free length ($l_{0,new}$)	310.8 mm
* Data given by GM ** Measured by UW for rear coil spring part number 23341853 Code AAZ6	

4.3 New Spring Parameters

Technical parameters for the new coil springs are defined based on the desired length and rate. In addition, the new springs need to have the same or close outer spring diameter, rod diameter and pitch for a proper fit with the stock spring isolators. In collaboration with a local custom spring manufacturer all technical parameters are determined as in **Table 4-4**. The springs are available at a price of $250 for the pair. A photograph comparing GM's stock spring and the new coil spring can be found in **Figure A-6**.

Table 4-4: New spring geometry parameters

Parameter	Value
Wire diameter	**0.5620 inches**
Minimum tensile strength	231.211 ksi
Wire length	80.1530 inches
Wire weight	5.64677 lb
Natural frequency	130 Hz
Coil ID	2.6860 inches
Coil OD	**3.8100 inches**
Total coils	7.75
Pitch	1.9315 inches
Pitch Angle	10.7186 degrees

4.4 Conclusions of Spring Calculations

1. The natural frequency and ride height of the vehicle's sprung mass can easily be adjusted through the coil spring rate and length.
2. The UW Camaro's 28.2% increase in rear axle vehicle mass leads to a 46.9% increase of desired spring rate and a 4.3% decrease for the free length.

4.5 Future Work for the Suspension

At this point no further suspension modifications are planned for the UW Camaro. The vehicle performed very competitively in the "ride quality" and "handling" dynamic events during the EcoCAR 3 Year 3 Competition, finishing 3rd in both events. The design of new springs should be considered if vehicle mass reduction efforts during Year 4 lead to significant changes in mass and its distribution.

BIBLIOGRAPHY

[1] K. De La Rosa, "EcoCAR 3: About," [Online]. Available: http://ecocar3.org/about/. [Accessed 10 4 2017].

[2] Gamma Technologies LLC, "gtisoft.com," Fresh Design Studio, 2017. [Online]. Available: https://www.gtisoft.com/gt-suite-applications/propulsion-systems/gt-power-engine-simulation-software/. [Accessed 24 4 2017].

[3] Gamma Technologies LLC, *GT-SUITE Engine Performance Tutorials,* Westmont, IL: Gamma Technologies LLC, 20107.

[4] S. a. F. P. Chen, *Development of a Single Cylinder Compression Ignition Research Engine, SAE Technical Paper 650733,* SAE International, 1965.

[5] G. Technologies, *GT-SUITE Engine Performance Application Manual VERSION 2017,* Westmont, IL: Gamma Technologies, 2016.

[6] J. B. Heywood, Internal Combustion Engine Fundamentals, New York: McGraw-Hill, Inc., 1988.

[7] S. Metals, "http://www.speedymetals.com," [Online]. Available: http://www.speedymetals.com/information/material64.html. [Accessed 15 4 2017].

[8] H. S. F. A. E. Seherr-Thoss, Universal Joints and Driveshafts, Analysis, Design, Applications, Berlin: Springer, 2006.

[9] W. D. P. P. D. F. Pilkey, Peterson's Stress Concentration Factors, Hoboken, New Jersey: John Wiley & Sons, Inc., 2008.

[10] A. H. Committee, "Steel Selection for Hardening," in *ASM Handbook, Vol 4D, Steel Selection for Hardening, Heat Treating of Irons and Steels*, ASM International, 2014, pp. 29-43.

[11] T. M. T. Philip, "Ultrahigh-Strength Steels, Medium-Carbon Low-Alloy Steels," in *ASM Handbook, Vol 1, Ultrahigh-Strength Steels, Properties and Selection: Irons, Steels, and High-Performance Alloys*, ASM International, 1990, p. p 430–448.

[12] A. H. Committee, "Hardness Conversions for Steels," in *ASM Handbook, Vol 8, Hardness Conversions for Steels, Mechanical Testing and Evaluation*, ASM International, 2000, p. 282–287.

[13] A. H. Committee, "Hardenability Curves," in *ASM Handbook, Vol 1, Hardenability Curves, Properties and Selection: Irons, Steels, and High-Performance Alloys*, ASM International, 1990, pp. 485-570.

[14] A. International, "Chapter 14 Fatigue," in *Elements of Metallurgy and Engineering Alloys*, ASM International, 2008, pp. 243-265.

[15] R. G. N. J. K. Budynas, "Fatigue Failure Resulting," in *SHIGLEY'S MECHANICAL ENGINEERING DESIGN, NINTH EDITION*, New York, McGraw-Hill, 2011, pp. 256-344.

[16] A. International, "Fatigue Resistance of Steels," in *ASM Handbook, Volume 1: Properties and Selection: Iron, Steels, and High-Performance Alloys*, ASM International, pp. 673-688.

[17] J. Y. Wong, "Vehicle Ride Characteristics," in *Theory of Ground Vehicles, 2nd Edition*, New York, John Wiley & Sons, Inc., 1993, p. 358.

A APPENDIX

A.1 Detailed Gearbox Design

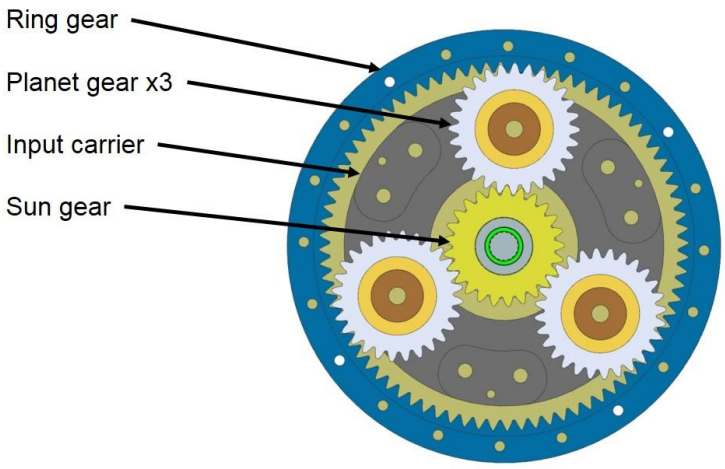

Figure A-1: Open gearbox showing planetary design with 3 planet gears

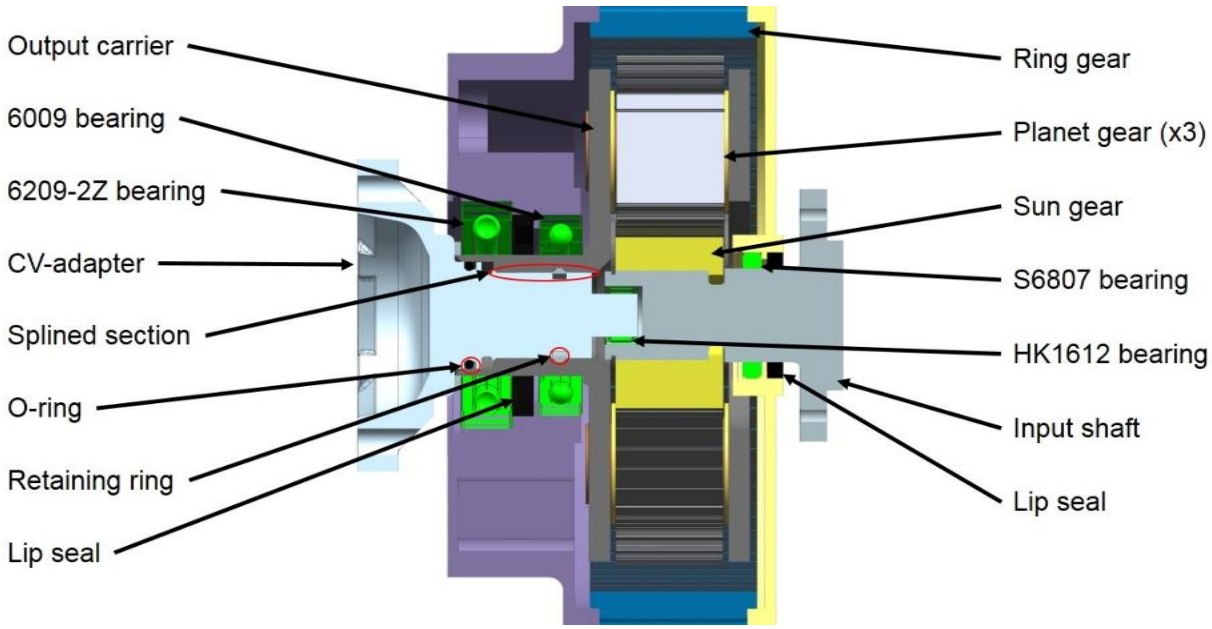

Figure A-2: Gearbox cross-section view with details for CV-adapter part

A.2 Honda VFR 800 Engine in GT-Power

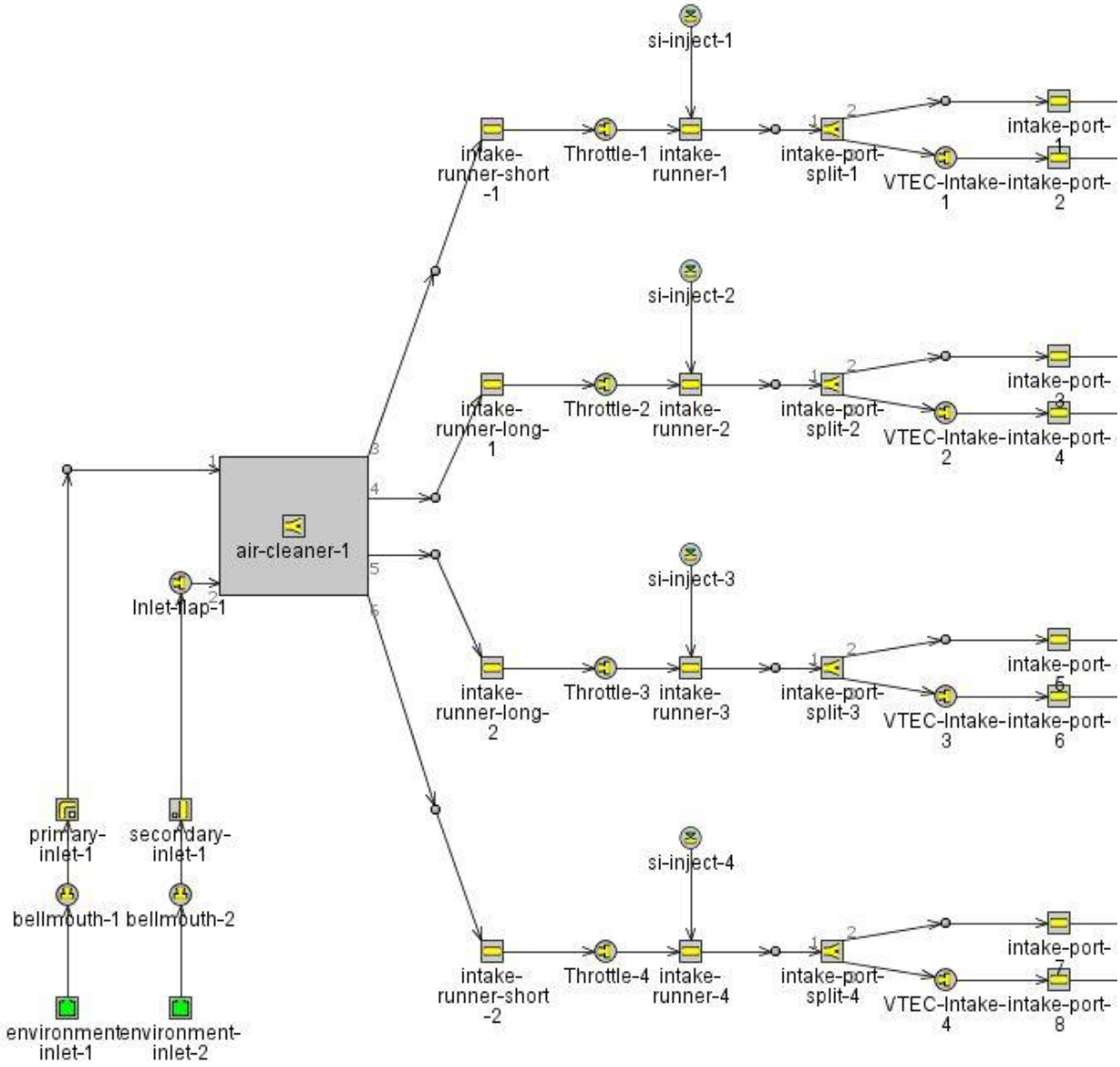

Figure A-3: Air intake system

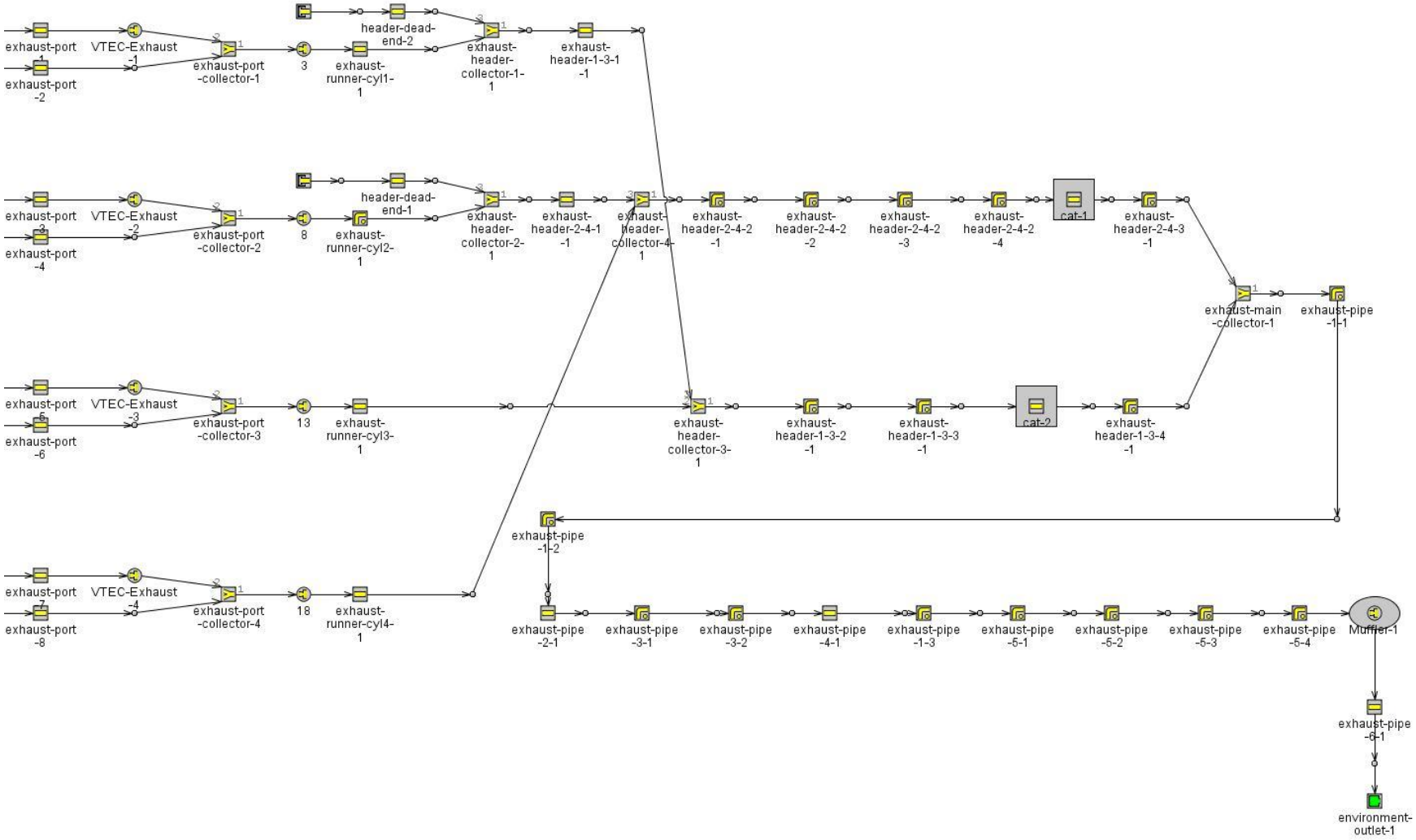

Figure A-4: Exhaust system

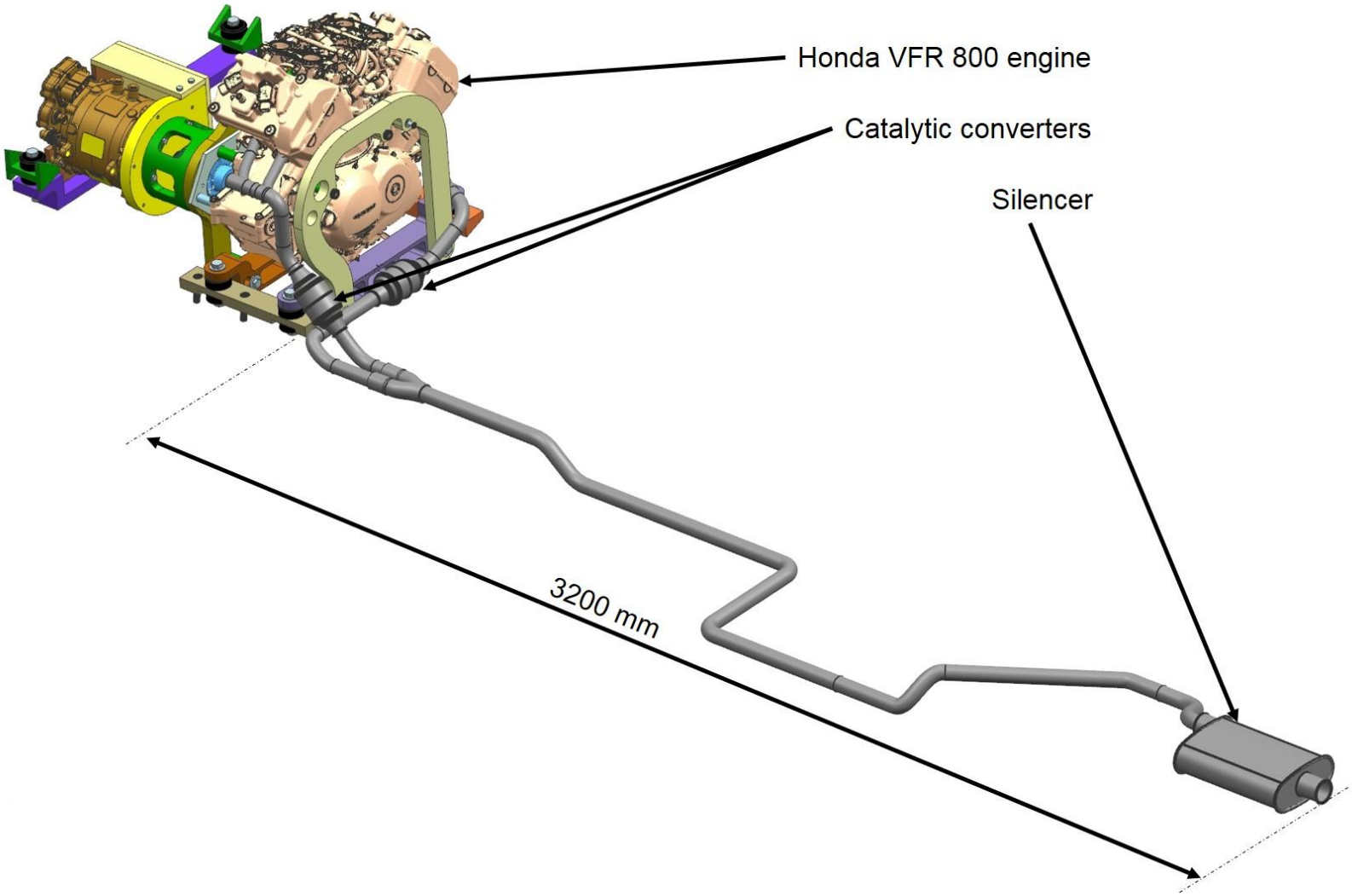

Figure A-5: UW Camaro exhaust system in CAD

A.3 New and Stock Coil Springs

Figure A-6: Stock and custom rear coil spring for Chevrolet Camaro